

**RESEARCH ARTICLE**

# Virtual elements on agglomerated finite elements to increase the critical time step in elastodynamic simulations

N. Sukumar<sup>\*,1</sup> | Michael R. Tupek<sup>2</sup>

<sup>1</sup>Department of Civil and Environmental Engineering, University of California, Davis, CA 95616, USA

<sup>2</sup>Sandia National Laboratories, Albuquerque, NM 87185, USA

**Correspondence**

\*N. Sukumar, Department of Civil and Environmental Engineering, University of California, One Shields Avenue, Davis, CA 95616, USA

Email: nsukumar@ucdavis.edu

In this paper, we use the first-order virtual element method (VEM) to investigate the effect of shape quality of polyhedra in the estimation of the critical time step for explicit three-dimensional elastodynamic finite element (FE) simulations. Low-quality finite elements are common when meshing realistic complex components, and while tetrahedral meshing technology is generally robust, meshing algorithms cannot guarantee high-quality meshes for arbitrary geometries or for non-water-tight computer-aided design models. For reliable simulations on such meshes, we consider FE meshes with tetrahedral and prismatic elements that have badly-shaped elements—tetrahedra with dihedral angles close to  $0^\circ$  and  $180^\circ$ , and slender prisms with triangular faces that have short edges—and agglomerate such ‘bad’ elements with neighboring elements to form a larger polyhedral virtual element. On each element, the element-eigenvalue inequality is used to estimate the critical time step. For a suite of illustrative finite element meshes with  $\epsilon$  being a mesh-coordinate parameter that leads to poor mesh quality, we show that adopting VEM on the agglomerated polyhedra yield critical time steps that are insensitive as  $\epsilon \rightarrow 0$ . The significant reduction in solution time on meshes with agglomerated virtual elements vis-à-vis tetrahedral meshes is demonstrated through explicit dynamics simulations on a tapered beam.

**KEYWORDS:**

VEM; consistency; hourglass stability; critical time step; sliver tetrahedron; linear elastodynamics

## 1 | INTRODUCTION

Over the past fifteen years there has been a sustained effort in the development of new finite element formulations on meshes consisting of arbitrary polytopal (polygonal and polyhedral) elements.<sup>1</sup> The virtual element method (VEM)<sup>2</sup> is a recent contribution in higher order stable Galerkin discretizations on polytopal meshes to solve boundary-value problems. It has its roots

in mimetic finite-difference schemes that are based on an algebraic construction for the system (stiffness, mass) matrices.<sup>3</sup> The VEM endows a variational framework for the first-order mimetic scheme, and in doing so, it provides a route to many new formulations. In the VEM, the basis functions are defined as the solution of a local elliptic partial differential equation, and are never explicitly computed in the implementation of the method. For this reason, they are referred to as *virtual*, and the finite element space of the VEM as the *virtual element space*. As in the finite element method (FEM), the local discretization space  $V_k(E)$  ( $k$  is the order of the element  $E$ ) from each element is glued together to form the conforming global space  $V^h$ . However, distinct from the standard FEM, the trial and test functions in  $V_k(E)$  consist of polynomials of order less than or equal to  $k$  and of additional nonpolynomial functions. Since the virtual basis functions are unknown in  $V_k(E)$ , the VEM uses their elliptic polynomial projections to build the bilinear form (stiffness and mass matrices) and the continuous linear functional (forcing terms) of the variational formulation. For problems such as the Poisson equation or linear elastostatics, such projections are computable from the degrees of freedom without introducing any further approximation error and are used to decompose the bilinear form on each element into two parts: the consistent term that approximates the stiffness matrix on a given polynomial space and the correction term that ensures coercivity (stability with the proper scaling). As in the FEM, element-level assembly procedures are used to obtain the global system matrices. For a simplex in  $\mathbb{R}^d$ , the first-order ( $k = 1$ ) VEM is identical to linear FEM. The VEM can be viewed as a stabilized hourglass control finite element method<sup>4</sup> on convex and nonconvex polytopes.<sup>5</sup>

In comparison to the standard finite element method, the simplicity and flexibility of the VEM has attracted attention from both applied mathematicians and engineers who have furthered the theory and applications of the method. The ability to devise accurate and stable numerical simulations on polygonal and polyhedral meshes with arbitrarily-shaped convex and nonconvex elements has led to many new applications of the method. Initially, the emphasis of the virtual element method was on low- and high-order formulations for two- and three-dimensional scalar elliptic problems.<sup>6,7,8,9</sup> Over the past five years, greater emphasis has been placed on vectorial problems such as fluid flow, and linear and nonlinear deformation of solids. Among these, we mention applications of the VEM in linear elastostatics,<sup>10,11,12,13</sup> linear elastodynamics,<sup>14,15,16</sup> and finite strain elastodynamics<sup>17</sup> that are pertinent to this contribution. Park et al.<sup>14,15</sup> were the first to show that the first-order VEM with explicit time integration is accurate and converges optimally for linear elastodynamic simulations over convex and nonconvex polygonal and polyhedral meshes. Antonietti et al.<sup>16</sup> proved stability and convergence of the semi-discrete arbitrary-order virtual element method for two-dimensional linear elastodynamic problems, and Cihan et al.<sup>17</sup> extended the low-order virtual element method for two- and three-dimensional finite strain elastodynamic simulations.

Low-quality finite elements are common when meshing realistic complex components, and while tetrahedral meshing technology is generally robust, meshing algorithms cannot guarantee high-quality meshes for arbitrary geometries or for non-water-tight computer-aided design models.<sup>18</sup> In explicit linear elastodynamic computations, the presence of tetrahedral slivers (dihedral angles close to  $0^\circ$  and  $180^\circ$ ) in a finite element mesh dramatically decreases the critical time step, making simulation progress

practically impossible. In this paper, we use the first-order VEM to investigate the effect of shape quality of polyhedra (formed via agglomeration of poor-quality elements in tetrahedral-dominant finite element meshes) in the estimation of the critical time step for explicit dynamics simulations. Agglomeration of tetrahedral elements to form polyhedra have been introduced for discontinuous Galerkin simulations,<sup>19,20</sup> and more recently in polyhedral finite element computations over tetrahedral meshes.<sup>21</sup> The structure of the remainder of this paper follows. The elastodynamic eigenproblem (strong and weak forms) is presented in Section 2. In Section 3, we present some of the essentials on polynomial basis sets and projection operators. Then, in Section 4, the main concepts in the VEM—definition of the virtual element space and degrees of freedom—are presented. The discrete generalized eigenproblem is also stated. In Section 5, the numerical implementation of three-dimensional VEM for linear solid mechanics problems is presented, including expressions for the element stiffness and element mass matrices, and details on the numerical integration using the homogeneous numerical integration scheme. It is known that triangles with an internal angle close to  $180^\circ$  (flat triangles) adversely affect interpolation accuracy, whereas an internal angle close to  $0^\circ$  (and the others not large) worsen stiffness-matrix conditioning.<sup>22</sup> The dihedral angle in a tetrahedron dictates element quality from the viewpoints of interpolation and stiffness-matrix conditioning.<sup>23</sup> Establishing such shape quality measures for polygons and polyhedra is challenging.<sup>24,25</sup> In the numerical results presented in Section 6, we consider polyhedral elements that are formed by agglomerating bad-quality tetrahedral elements (small edges, small faces, dihedral angles close to  $0^\circ$  and  $180^\circ$ ) with neighboring tetrahedra of good quality. We refer to such an element as a *polyhedral virtual element*. The elastodynamic eigenproblem on each element is solved, and the element eigenvalue inequality<sup>26,27,28</sup> is used to obtain a lower bound estimate of the critical time step. Comparisons of the critical time step on a suite of bad-quality tetrahedral finite elements are made with a polyhedral virtual element to assess the performance of the VEM. Finally, we present explicit dynamics simulations on a three-dimensional tapered beam to demonstrate that the increase in critical time step using polyhedral virtual elements leads to significantly faster computer simulations when compared to tetrahedral finite elements. We close with a summary of our main findings and conclusions in Section 7.

## 2 | STRONG AND WEAK FORMS OF THE THREE-DIMENSIONAL LINEAR ELASTODYNAMIC EIGENPROBLEM

The motion of waves in a linearly elastic solid is governed by the equations of elastodynamics. The governing field equations in a domain  $\Omega \subset \mathbb{R}^3$  are:

$$\nabla \cdot \boldsymbol{\sigma} = \rho \ddot{\mathbf{u}}, \quad \boldsymbol{\sigma} = \boldsymbol{\sigma}^T \quad (\text{balance of linear and angular momentum}), \quad (1a)$$

$$\boldsymbol{\sigma} = \mathbb{C} : \boldsymbol{\varepsilon} \quad (\text{linear elastic constitutive law}), \quad (1b)$$

$$\boldsymbol{\varepsilon} = \frac{1}{2} (\nabla \mathbf{u} + (\nabla \mathbf{u})^T) \quad (\text{small-strain kinematics}), \quad (1c)$$

where  $\boldsymbol{\sigma} := \boldsymbol{\sigma}(\mathbf{x}, t)$  is the Cauchy stress,  $\rho := \rho(\mathbf{x})$  is the density,  $\mathbf{u} := \mathbf{u}(\mathbf{x}, t)$  is the displacement field,  $\boldsymbol{\varepsilon} := \boldsymbol{\varepsilon}(\mathbf{x}, t)$  is the strain field, and  $\mathbb{C}$  is the linear elastic material moduli tensor. Assuming time-harmonic fields with angular frequency  $\omega$ , the field quantities can be decomposed to yield

$$\mathbf{u}(\mathbf{x}, t) = \mathbf{u}(\mathbf{x}) \exp(-i\omega t), \quad \boldsymbol{\sigma}(\mathbf{x}, t) = \boldsymbol{\sigma}(\mathbf{x}) \exp(-i\omega t), \quad \boldsymbol{\varepsilon}(\mathbf{x}, t) = \boldsymbol{\varepsilon}(\mathbf{x}) \exp(-i\omega t). \quad (2)$$

Combining (1) and (2), we obtain the elastodynamic eigenproblem for free vibrations:

$$\nabla \cdot \boldsymbol{\sigma}(\mathbf{x}) = -\lambda \rho(\mathbf{x}) \mathbf{u}(\mathbf{x}) \quad \text{in } \Omega, \quad (3a)$$

where  $\lambda = \omega^2$  is the eigenvalue, and homogeneous displacement boundary conditions are imposed on the boundary:

$$\mathbf{u} = \mathbf{0} \quad \text{on } \partial\Omega. \quad (3b)$$

The weak form of the eigenproblem in (3) is: find the displacement field (trial eigenfunction)  $\mathbf{u} \in V = [H_0^1(\Omega)]^3$  and eigenvalue  $\lambda = \omega^2 \in \mathbb{R}_+$ , such that

$$a(\mathbf{u}, \mathbf{v}) = \lambda b(\mathbf{u}, \mathbf{v}) \quad \forall \mathbf{v} \in V, \quad (4a)$$

where  $\mathbf{v}$  is the test displacement field,  $H_0^1(\Omega)$  is the Hilbert space that consists of functions in  $\Omega$  that have square integrable derivatives up to order 1 and which vanish on  $\partial\Omega$ , and the bilinear forms  $a(\cdot, \cdot)$  and  $b(\cdot, \cdot)$  are given by

$$a(\mathbf{u}, \mathbf{v}) := \int_{\Omega} \boldsymbol{\sigma}(\mathbf{u}) : \boldsymbol{\varepsilon}(\mathbf{v}) \, d\mathbf{x}, \quad b(\mathbf{u}, \mathbf{v}) := \int_{\Omega} \rho \mathbf{u} \cdot \mathbf{v} \, d\mathbf{x}. \quad (4b)$$

### 3 | MATHEMATICAL PRELIMINARIES

#### 3.1 | Polynomial basis

Let  $\Omega \subset \mathbb{R}^d$  ( $d = 2, 3$ ) be the problem domain, and  $\mathcal{T}^h$  a decomposition of  $\Omega$  into nonoverlapping *simple* polygons or polyhedra. The number of nodes in  $\mathcal{T}^h$  is  $N$ . This definition for the elements permits the inclusion of elements with consecutive coplanar edges and faces. We refer to  $E \in \mathcal{T}^h$  as an *element*. Let  $|E|$  be the area in 2D and volume in 3D of  $E$ . The diameter of  $E$  is

denoted by  $h_E$  and  $\mathbf{x}_E$  is the centroid (barycenter) of  $E$ . The vertices of  $E$  are denoted by  $v_i$ , and the coordinate of vertex  $v_i$  by  $\mathbf{x}_i \equiv (x_i, y_i)$  in 2D and  $\mathbf{x}_i \equiv (x_i, y_i, z_i)$  in 3D. A polygon  $E$  has  $N_E$  vertices and  $N_E$  edges, with the edges denoted by  $e_i$  ( $i = 1, 2, \dots, N_E$ ). In 3D, a polyhedron  $E$  has  $N_E$  vertices, and is described by its faces (each is assumed to be a planar polygon) that are labeled as  $\mathbf{f}_i$  ( $i = 1, 2, \dots, N_E^f$ ), where  $N_E^f$  is the number of faces of the polyhedron. Each face  $\mathbf{f}_i$  is given by a vertex connectivity in counter-clockwise orientation such that the normal to the face points out of  $E$ .

Let  $\mathbb{P}_k(E)$  be the function space on  $E$  that consists of all polynomials of order less than or equal to  $k$ . By convention,  $\mathbb{P}_{-1} = \{0\}$ . The dimension of  $\mathbb{P}_k(E)$  is denoted by  $\dim \mathbb{P}_k(E)$ . In one dimension,  $\dim \mathbb{P}_k(E) = k + 1$ ; in two dimension,  $\dim \mathbb{P}_k(E) = (k + 1)(k + 2)/2$ , and in three dimension,  $\dim \mathbb{P}_k(E) = (k + 1)(k + 2)(k + 3)/6$ . The set consisting of the scaled monomials of order less than or equal to  $k$  on  $E$  is defined as  $\mathcal{M}_k(E)$ . For example, in two dimensions

$$\mathcal{M}_1(E) = \left\{ 1, \frac{x - x_E}{h_E}, \frac{y - y_E}{h_E} \right\},$$

and in three dimension

$$\mathcal{M}_1(E) = \left\{ 1, \frac{x - x_E}{h_E}, \frac{y - y_E}{h_E}, \frac{z - z_E}{h_E} \right\}$$

are scaled monomial basis sets of order 1. Note that  $\mathcal{M}_1(E)$  is a basis for  $\mathbb{P}_1(E)$ , and all elements of  $\mathcal{M}_1(E)$  are  $\mathcal{O}(1)$ . The scaled monomial basis set is used in the virtual element computations for scalar problems. In the literature,  $m_\alpha$  is used to refer to an element of  $\mathcal{M}_k(E)$ , and  $\mathcal{M}_k^*(E)$  is used to denote the basis set on  $E$  that contains all monomials that are exactly of order  $k$ .

Let  $\mathbf{P}_1(E) = \mathbb{P}_1(E) \otimes \mathbf{I}_d$  ( $\mathbf{I}_d$  is the  $d \times d$  identity matrix and  $\otimes$  is the Kronecker product) be the vector polynomial basis defined on  $E$ , and  $\mathbf{P}_1^*(E)$  denote the vector polynomial basis on  $E$  that is exactly of order 1. For linear elasticity or linear elastodynamics, there are three rigid-body modes in 2D and six rigid-body modes in 3D. These are also known as zero-energy modes. Let

$$\xi := \frac{x - x_E}{h_E}, \quad \eta := \frac{y - y_E}{h_E}, \quad \zeta := \frac{z - z_E}{h_E}. \quad (5)$$

For solid continua, we use a suitable scaled vectorial basis set (first order,  $k = 1$ ) in 2D and 3D. In two dimensions,

$$\mathbf{M}^{\text{RBM}}(E) = \left[ \begin{array}{c} \left\{ 1 \right\} \\ \left\{ 0 \right\} \\ \left\{ 0 \right\} \end{array} \right], \quad \widehat{\mathbf{M}}(E) := \mathbf{M}_1(E) = \mathbf{M}^{\text{RBM}}(E) \cup \left[ \begin{array}{c} \left\{ \eta \right\} \\ \left\{ \xi \right\} \\ \left\{ 0 \right\} \end{array} \right], \quad (6a)$$

and in three dimensions,

$$\mathbf{M}^{\text{RBM}}(E) = \left[ \begin{array}{c} \left[ \begin{array}{c} 1 \\ 0 \\ 0 \end{array} \right], \left[ \begin{array}{c} 0 \\ 1 \\ 0 \end{array} \right], \left[ \begin{array}{c} 0 \\ 0 \\ 1 \end{array} \right], \left[ \begin{array}{c} 0 \\ -\zeta \\ \eta \end{array} \right], \left[ \begin{array}{c} \zeta \\ 0 \\ -\xi \end{array} \right], \left[ \begin{array}{c} -\eta \\ \xi \\ 0 \end{array} \right] \end{array} \right],$$

$$\widehat{\mathbf{M}}(E) := \mathbf{M}_1(E) = \mathbf{M}^{\text{RBM}}(E) \cup \left[ \begin{array}{c} \left[ \begin{array}{c} 0 \\ \zeta \\ \eta \end{array} \right], \left[ \begin{array}{c} \zeta \\ 0 \\ \xi \end{array} \right], \left[ \begin{array}{c} \eta \\ \xi \\ 0 \end{array} \right], \left[ \begin{array}{c} \xi \\ 0 \\ 0 \end{array} \right], \left[ \begin{array}{c} 0 \\ \eta \\ 0 \end{array} \right], \left[ \begin{array}{c} 0 \\ 0 \\ \zeta \end{array} \right] \end{array} \right], \quad (6b)$$

where  $\mathbf{M}^{\text{RBM}}(E)$  contains the rigid body modes (vectors). Now,  $\widehat{\mathbf{M}}(E)$  is a basis for  $\mathbf{P}_1(E)$ , and we use  $\mathbf{m}_\alpha$  to refer to a vector element of  $\widehat{\mathbf{M}}(E)$ . Further, we use  $\widehat{\mathbf{M}}^*(E)$  to denote the basis set for a vector field on  $E$  that contains all scaled vector monomials that are exactly of order 1.

### 3.2 | Polynomial projection operators

We use standard Sobolev spaces,  $L^2(E)$  and  $H^1(E)$ , on element  $E$  with usual definitions for inner products and norms (semi-norms) for functions that belong to these spaces. Since only  $k = 1$  is considered in this paper, we let  $\Pi^0 \equiv \Pi_{E,1}^0$ ,  $\Pi^\nabla \equiv \Pi_{E,1}^\nabla$ , and  $\Pi^\epsilon \equiv \Pi_{E,1}^\epsilon$  be the  $L^2$ , elliptic (Laplacian), and strain energy (solid continua) projection operators.

**$L^2$  Projection Operator:** For a vector field  $\mathbf{v} \in [L^2(E)]^d$ , define the  $L^2$  orthogonal projection operator  $\Pi^0 : [L^2(E)]^d \rightarrow \mathbf{P}_1(E)$  such that  $\Pi^0 \mathbf{v}$  is the unique element in  $\mathbf{P}_1(E)$  that satisfies

$$(\mathbf{q}, \mathbf{v} - \Pi^0 \mathbf{v})_E = 0 \quad \forall \mathbf{q} \in \mathbf{P}_1(E), \quad (7)$$

where  $(\cdot, \cdot)_E$  is the standard  $L^2$  inner product over  $E$ .

**Elliptic (Vector Laplacian) Projection Operator:** For a vector-valued function  $\mathbf{v} \in [H^1(E)]^d$  and the inner product (bilinear form) associated with the vector Laplacian,  $a_E(\mathbf{u}, \mathbf{v}) = \int_E \nabla \mathbf{u} : \nabla \mathbf{v} \, d\mathbf{x}$ , define the vectorial elliptic orthogonal projection operator  $\Pi^\nabla : [H^1(E)]^d \rightarrow \mathbf{P}_1(E)$  such that  $\Pi^\nabla \mathbf{v}$  is the unique element in  $\mathbf{P}_1(E)$  that satisfies

$$\begin{cases} a_E(\mathbf{q}, \mathbf{v} - \Pi^\nabla \mathbf{v}) = 0 & \forall \mathbf{q} \in \mathbf{P}_1(E), \\ \int_{\partial E} (\mathbf{v} - \Pi^\nabla \mathbf{v}) \, dS = \mathbf{0}. \end{cases} \quad (8)$$

**Energy Projection Operator for Solid Continua:** Let  $\mathbf{u}, \mathbf{v} \in [H^1(E)]^3$  be vector-valued functions and  $[\mathbb{P}_1(E)]_{\text{sym}}^{3 \times 3}$  be the space of order 1 polynomial second-order symmetric tensors. The internal virtual work for a deformable solid is:

$$a_E(\mathbf{u}, \mathbf{v}) = \int_E \boldsymbol{\sigma}(\mathbf{u}) : \boldsymbol{\varepsilon}(\mathbf{v}) \, d\mathbf{x}, \quad (9)$$

where  $\mathbf{u}$  is the trial displacement field,  $\mathbf{v}$  is the test (virtual) displacement field, and  $\boldsymbol{\varepsilon}(\mathbf{v})$  and  $\boldsymbol{\sigma}(\mathbf{u})$  are the virtual strain tensor and Cauchy stress tensor, respectively.

If  $\mathbf{u}$  is a vector polynomial of order 1, then  $\boldsymbol{\varepsilon}(\mathbf{u}) = \nabla_s(\mathbf{u}) \in [\mathbb{P}_0(E)]_{\text{sym}}^{3 \times 3}$  is a constant symmetric second-order tensor ( $\nabla_s$  is the symmetric gradient operator) and so is  $\boldsymbol{\sigma}(\mathbf{u})$ . We define the projection operator  $\Pi^\varepsilon : [H^1(E)]^3 \rightarrow \mathbf{P}_1(E)$  such that  $\Pi^\varepsilon \mathbf{v} \in \mathbf{P}_1(E)$ , whereas  $\Pi^\varepsilon \boldsymbol{\varepsilon} \in [\mathbb{P}_0(E)]_{\text{sym}}^{3 \times 3}$ . For first order consistency, we require that  $(\mathbf{v} - \Pi^\varepsilon \mathbf{v})$  is orthogonal to all vector polynomials in the energy inner product defined in (9):

$$a_E(\mathbf{m}_\alpha, \mathbf{v} - \Pi^\varepsilon \mathbf{v}) = 0 \quad \forall \mathbf{m}_\alpha \in \widehat{\mathbf{M}}(E). \quad (10a)$$

Referring to (6), observe that for  $\mathbf{m}_\alpha \in \mathbf{M}^{\text{RBM}}(E)$ , we have  $\boldsymbol{\varepsilon}(\mathbf{m}_\alpha) = \mathbf{0}$ , and therefore  $\boldsymbol{\sigma}(\mathbf{m}_\alpha) = \mathbf{C} : \boldsymbol{\varepsilon}(\mathbf{m}_\alpha) = \mathbf{0}$ . Hence, for such  $\mathbf{m}_\alpha$ , (10a) yields the trivial identity  $0 = 0$ , and hence we provide additional conditions to fully determine the coefficients of the vector polynomial that correspond to the rigid-body modes. For  $k = 1$ , we use<sup>10</sup>

$$\int_{\partial E} (\mathbf{v} - \Pi^\varepsilon \mathbf{v}) \cdot \mathbf{m}_\alpha \, dS = \mathbf{0}, \quad (10b)$$

where  $\alpha = 1-3$  in 2D and  $\alpha = 1-6$  in 3D.

## 4 | VIRTUAL ELEMENT METHOD FOR SOLID CONTINUA

Let  $V(E)$  denote the first-order ( $k = 1$ ) virtual element space on a three-dimensional element  $E$  and  $V(\mathbf{f})$  be the first-order virtual element space on a particular face  $\mathbf{f}$  of  $E$ . First, the virtual element space in two dimensions is described and then the virtual element space in three dimensions. Other key elements such as the degrees of freedom, and the construction of the bilinear forms for the internal virtual work and the inertial virtual work are also presented. Finally, the numerical implementation of the method (computation of consistency and stability parts of the stiffness and mass matrices) is described. The exposition draws on the presentations that appear in the literature.<sup>7,5,13,29</sup>

### 4.1 | Definition of the space $V(F)$ for $d = 2$

Let  $F$  be an element in two dimensions. We point out that in Section 4.2, we use  $\mathbf{f}$  (two-dimensional polygon) to represent a face of a three-dimensional element  $E$ . For a vectorial problem, the (enhanced) virtual element space  $V(F)$  in two dimensions is defined as:<sup>6</sup>

$$V(F) = \left\{ \mathbf{v}^h : \mathbf{v}^h \in [H^1(F)]^2, \Delta \mathbf{v}^h \in \mathbf{P}_1(F), \mathbf{v}^h|_e \in \mathbf{P}_1(e) \forall e \in \partial F, \right. \\ \left. \mathbf{v}^h|_{\partial F} \in [C^0]^2(\partial F), \int_F \mathbf{v}^h \cdot \mathbf{q} \, d\mathbf{x} = \int_F \Pi_F^\nabla \mathbf{v}^h \cdot \mathbf{q} \, d\mathbf{x} \quad \forall \mathbf{q} \in \mathbf{P}_0^*(F) \cup \mathbf{P}_1^*(F) \right\}. \quad (11)$$

In two dimensions, a vector-valued function  $\mathbf{v}^h \in V(F)$  is characterized by the following properties:

- (i)  $\mathbf{v}^h$  is such that each component is continuous and piecewise linear on  $\partial F$ .
- (ii)  $\Delta \mathbf{v}^h$  is a linear vector polynomial, where  $\Delta$  is the vector Laplacian.
- (iii)  $\int_F \mathbf{v}^h \cdot \mathbf{q} \, d\mathbf{x} = \int_F \Pi_F^\nabla \mathbf{v}^h \cdot \mathbf{q} \, d\mathbf{x}$  for all linear vector polynomials  $\mathbf{q}$ , where  $\Pi_F^\nabla$  is the elliptic projector in  $F$ .

Note that the second condition is distinct from the one introduced in Beirão et al<sup>2</sup> for the Poisson problem ( $\Delta v^h = 0$ ). In addition, the third condition states that  $\Pi_F^\nabla \mathbf{v}^h$  is also the  $L^2$ -projection of  $\mathbf{v}^h$  onto linear vector polynomials for  $k = 1$ .<sup>6</sup> In essence, the second condition adds three additional degrees of freedom in each dimension (Laplacian of a scalar field is an affine function) and the third condition provides an equation to compute them. These two modifications enable the computations in 3D (integrals over polygonal faces of the polyhedra) to be performed using only the values of  $\mathbf{v}^h$  at the vertices of  $E$ .

## 4.2 | Definition of the space $V(E)$ for $d = 3$

For a vectorial problem, the (enhanced) virtual element space  $V(E)$  in three dimensions is defined as:<sup>6</sup>

$$V(E) = \left\{ \mathbf{v}^h : \mathbf{v}^h \in [H^1(E)]^3, \Delta \mathbf{v}^h \in \mathbf{P}_1(E), \mathbf{v}^h|_{\mathfrak{f}} \in V(\mathfrak{f}) \forall \mathfrak{f} \in \partial E, \int_E \mathbf{v}^h \cdot \mathbf{q} \, d\mathbf{x} = \int_E \Pi_E^\nabla \mathbf{v}^h \cdot \mathbf{q} \, d\mathbf{x} \forall \mathbf{q} \in \mathbf{P}_0^*(E) \cup \mathbf{P}_1^*(E) \right\}. \quad (12)$$

In three dimensions, a function  $\mathbf{v}^h \in V(E)$  is characterized by the following properties:

- (i)  $\mathbf{v}^h$  is continuous and unknown inside  $E$ , and in general also unknown on  $\partial E$ .
- (ii)  $\mathbf{v}^h$  is such that its restriction to a face  $\mathfrak{f}$  belongs to  $V(\mathfrak{f})$  as defined in (11).
- (iii)  $\Delta \mathbf{v}^h$  is a linear vector polynomial.
- (iv)  $\int_E \mathbf{v}^h \cdot \mathbf{q} \, d\mathbf{x} = \int_E \Pi_E^\nabla \mathbf{v}^h \cdot \mathbf{q} \, d\mathbf{x}$  for all linear vector polynomials  $\mathbf{q}$ .

The global virtual element space  $V^h \subset [H_0^1(\Omega)]^3$  is defined using standard assembly procedures as in finite elements:

$$V^h = \{ \mathbf{v}^h \in [H_0^1(\Omega)]^3 : \mathbf{v}^h|_E \in V(E) \text{ for all } E \in \Omega^h \}. \quad (13)$$

## 4.3 | Degrees of freedom

To solve a vectorial problem using a first-order virtual element formulation ( $k = 1$ ), we take the values of  $\mathbf{v}^h$  at the vertices of the polyhedron as its degrees of freedom (DOFs). Let us associate a (virtual) canonical Lagrange basis,  $\phi_i(\mathbf{x})$  ( $i = 1, 2, \dots, N_E$ ),



to each vertex. The  $\phi_i(\mathbf{x})$  possesses the Kronecker-delta property, namely  $\phi_i(\mathbf{x}_j) = \delta_{ij}$ . In addition, they satisfy the constant and linear reproducing conditions:  $\sum_{i=1}^{N_E} \phi_i(\mathbf{x}) = 1$ ,  $\sum_{i=1}^{N_E} \phi_i(\mathbf{x})\xi_i = \xi$ ,  $\sum_{i=1}^{N_E} \phi_i(\mathbf{x})\eta_i = \eta$ , and  $\sum_{i=1}^{N_E} \phi_i(\mathbf{x})\zeta_i = \zeta$ . The total number of degrees of freedom in each element  $E$  is  $N_E^{\text{dofs}} = 3N_E$ . Let us define the vectorial basis function matrix:

$$\begin{aligned} \boldsymbol{\varphi} &:= \boldsymbol{\phi} \otimes \mathbf{I}_3 = \{\phi_1 \ \phi_2 \ \dots \ \phi_{N_E}\} \otimes \mathbf{I}_3 = \begin{bmatrix} \phi_1 & \phi_2 & \dots & \phi_{N_E} & 0 & 0 & \dots & 0 & 0 & 0 & \dots & 0 \\ 0 & 0 & \dots & 0 & \phi_1 & \phi_2 & \dots & \phi_{N_E} & 0 & 0 & \dots & 0 \\ 0 & 0 & \dots & 0 & 0 & 0 & \dots & 0 & \phi_1 & \phi_2 & \dots & \phi_{N_E} \end{bmatrix} \\ &:= \left[ \boldsymbol{\varphi}_1 \ \boldsymbol{\varphi}_2 \ \dots \ \boldsymbol{\varphi}_{N_E} \ \boldsymbol{\varphi}_{N_E+1} \ \boldsymbol{\varphi}_{N_E+2} \ \dots \ \boldsymbol{\varphi}_{2N_E} \ \boldsymbol{\varphi}_{2N_E+1} \ \boldsymbol{\varphi}_{2N_E+2} \ \dots \ \boldsymbol{\varphi}_{3N_E} \right], \end{aligned} \quad (14)$$

where  $\boldsymbol{\varphi}_i = \{\phi_i \ 0 \ 0\}^T$ ,  $\boldsymbol{\varphi}_{N_E+i} = \{0 \ \phi_i \ 0\}^T$ , and  $\boldsymbol{\varphi}_{2N_E+i} = \{0 \ 0 \ \phi_i\}^T$  for  $i = 1, \dots, N_E$ , are the  $3N_E$  vectorial basis functions. This choice can be seen as a natural generalization of the scalar problem to the vectorial case. We can write the interpolant of a vector-valued function  $\mathbf{v}(\mathbf{x})$  in  $E$  as:

$$\mathbf{v}^h(\mathbf{x}) = \sum_{i=1}^{3N_E} \boldsymbol{\varphi}_i(\mathbf{x}) v_i, \quad (15)$$

where each vectorial basis function is multiplied by a scalar coefficient. We can express (15) as

$$\mathbf{v}^h(\mathbf{x}) = \sum_{i=1}^{3N_E} \boldsymbol{\varphi}_i(\mathbf{x}) \text{dof}_i(\mathbf{v}^h), \quad (16)$$

where the operator  $\text{dof}_i(\mathbf{v}^h)$  extracts the  $i$ -th degree of freedom (scalar) of the vector field  $\mathbf{v}^h$ .

#### 4.4 | Discrete generalized eigenproblem

From the weak form of the continuous problem in (4), we can write the weak form for the VEM as: find  $\mathbf{u}^h \in V^h \subset V$  and  $\lambda \in \mathbb{R}_+$  such that

$$a^h(\mathbf{u}^h, \mathbf{v}^h) = \lambda b(\mathbf{u}^h, \mathbf{v}^h) \quad \forall \mathbf{v}^h \in V^h \subset V, \quad (17)$$

where  $a^h(\cdot, \cdot)$  and  $b^h(\cdot, \cdot)$  are the virtual element bilinear forms that approximate the exact bilinear forms  $a(\cdot, \cdot)$  and  $b(\cdot, \cdot)$ .

We define the discrete bilinear forms  $a^h(\mathbf{u}^h, \mathbf{v}^h)$  and  $b^h(\mathbf{u}^h, \mathbf{v}^h)$  for  $\mathbf{u}^h, \mathbf{v}^h \in V^h$  as the sum of elemental contributions

$$a^h(\mathbf{u}^h, \mathbf{v}^h) = \sum_{E \in \mathcal{T}^h} a_E^h(\mathbf{u}^h, \mathbf{v}^h), \quad b^h(\mathbf{u}^h, \mathbf{v}^h) = \sum_{E \in \mathcal{T}^h} b_E^h(\mathbf{u}^h, \mathbf{v}^h), \quad (18)$$

where the weak form on element  $E$  reads: find  $\mathbf{u}^h \in V(E)$  and  $\lambda_E \in \mathbb{R}_+$  such that

$$a_E^h(\mathbf{u}^h, \mathbf{v}^h) = \lambda_E b_E^h(\mathbf{u}^h, \mathbf{v}^h) \quad \forall \mathbf{v}^h \in V(E), \quad (19a)$$

$$a_E^h(\mathbf{u}^h, \mathbf{v}^h) = \int_E \boldsymbol{\sigma}(\mathbf{u}^h) : \boldsymbol{\varepsilon}(\mathbf{v}^h) \, d\mathbf{x}, \quad b_E^h(\mathbf{u}^h, \mathbf{v}^h) = \int_E \mathbf{u}^h \cdot \mathbf{v}^h \, d\mathbf{x}. \quad (19b)$$

Recall that  $\{\boldsymbol{\varphi}_i\}_{i=1}^{3N_E}$  are the canonical vectorial basis function on  $E$ . On expanding the trial and test functions as a linear combination of these basis functions and substituting them in (19), and using the arbitrariness of the test coefficients, we obtain the following generalized eigenproblem:

$$\mathbf{K}d = \lambda \mathbf{M}d, \quad \mathbf{K} = \sum_{E \in \mathcal{T}^h} \mathbf{K}_E, \quad \mathbf{M} = \sum_{E \in \mathcal{T}^h} \mathbf{M}_E, \quad (20a)$$

$$\mathbf{K}_E = a_E^h(\boldsymbol{\varphi}, \boldsymbol{\varphi}), \quad \mathbf{M}_E = b_E^h(\boldsymbol{\varphi}, \boldsymbol{\varphi}), \quad (20b)$$

where  $\mathbf{K}_E$  and  $\mathbf{K}$  are the element and global stiffness matrices,  $\mathbf{M}_E$  and  $\mathbf{M}$  are the element and global mass matrices, and the pair  $\{\lambda, d\}$  is the eigensolution. In the VEM,  $a_E^h(\cdot, \cdot)$  and  $b_E^h(\cdot, \cdot)$  consist of a consistency term and a stability term. These terms for the stiffness matrix are presented in (35) and those for the mass matrix appear in (44). Note that (19) is solved to compute the maximum element eigenvalue, which is used to bound the critical time step as shown in Section 5.4.

For convergence, the bilinear forms  $a_E^h(\cdot, \cdot)$  and  $b_E^h(\cdot, \cdot)$  must satisfy the following properties:<sup>2,30</sup>

- *linear consistency*: for all  $\mathbf{v}^h \in V(E)$  and linear vector polynomials  $\mathbf{q} \in \mathbf{P}_1(E)$  it holds that

$$a_E^h(\mathbf{q}, \mathbf{v}^h) = a_E(\mathbf{q}, \mathbf{v}^h), \quad (21a)$$

$$b_E^h(\mathbf{q}, \mathbf{v}^h) = (\mathbf{q}, \mathbf{v}^h)_E. \quad (21b)$$

- *stability*: there exists four positive constants  $\alpha_*, \alpha^*, \beta_*, \beta^*$ , independent of  $h$  and  $E$ , such that

$$\alpha_* a_E(\mathbf{v}^h, \mathbf{v}^h) \leq a_E^h(\mathbf{v}^h, \mathbf{v}^h) \leq \alpha^* a_E(\mathbf{v}^h, \mathbf{v}^h) \quad \forall \mathbf{v}^h \in V(E), \quad (22a)$$

$$\beta_* (\mathbf{v}^h, \mathbf{v}^h)_E \leq b_E^h(\mathbf{v}^h, \mathbf{v}^h) \leq \beta^* (\mathbf{v}^h, \mathbf{v}^h)_E \quad \forall \mathbf{v}^h \in V(E). \quad (22b)$$

## 5 | NUMERICAL IMPLEMENTATION

We derive the discrete system to compute the matrix representation of the energy projector  $\Pi^\epsilon$  and the  $L^2$  projector  $\Pi^0$ . Expressions are presented for the element stiffness matrix in three dimensions, and for the consistent and lumped mass matrices in both 2D and 3D. Finally, the main elements of the homogeneous numerical integration method are discussed.

### 5.1 | Computation of energy projection matrices

Referring to (14), let

$$\Pi^\epsilon \boldsymbol{\varphi}_i = \sum_{\beta=1}^{12} m_\beta s_\beta^i = \widehat{\mathbf{M}} s^i \quad (i = 1, 2, \dots, 3N_E) \quad (23)$$

be the projection of the vectorial canonical basis functions onto the scaled vector polynomial basis functions. In (23),  $s_\beta^i$  are unknown coefficients,  $\widehat{\mathbf{M}} := \widehat{\mathbf{M}}(E)$  is given in (6), and we have suppressed the spatial dependence of  $\boldsymbol{\varphi}_i$  and  $m_\alpha$ . Now, we can

write

$$\Pi^\epsilon \boldsymbol{\varphi} = \Pi^\epsilon \{ \boldsymbol{\varphi}_1 \ \boldsymbol{\varphi}_2 \ \dots \ \boldsymbol{\varphi}_{3N_E} \} = \sum_{\beta=1}^{12} \mathbf{m}_\beta \{ s_\beta^1 \ s_\beta^2 \ \dots \ s_\beta^{3N_E} \} := \widehat{\mathbf{M}} \mathbf{S} := \widehat{\mathbf{M}} \boldsymbol{\Pi}_*^\epsilon, \quad (24)$$

where  $\boldsymbol{\Pi}_*^\epsilon := \mathbf{S}$  is the matrix representation of the projection of the canonical shape functions with respect to the scaled vector monomial basis set  $\widehat{\mathbf{M}}$ .

Define the dof-matrix,  $\mathbf{D}$ , with entries  $\mathbf{D}_{i\alpha} = \text{dof}_i(\mathbf{m}_\alpha)$  as:

$$\mathbf{D} = \begin{bmatrix} \text{dof}_1(\mathbf{m}_1) & \text{dof}_1(\mathbf{m}_2) & \dots & \text{dof}_1(\mathbf{m}_{12}) \\ \text{dof}_2(\mathbf{m}_1) & \text{dof}_2(\mathbf{m}_2) & \dots & \text{dof}_2(\mathbf{m}_{12}) \\ \dots & \dots & \dots & \dots \\ \text{dof}_{3N_E}(\mathbf{m}_1) & \text{dof}_{3N_E}(\mathbf{m}_2) & \dots & \text{dof}_{3N_E}(\mathbf{m}_{12}) \end{bmatrix}, \quad (25)$$

where the operator  $\text{dof}_i(\cdot)$  is defined in (16). On using (6), (14) and (25), the constant and linear reproducing conditions can be written as:

$$\widehat{\mathbf{M}} = \boldsymbol{\varphi} \mathbf{D} = \mathbf{I} \otimes \{ \phi_1 \ \phi_2 \ \dots \ \phi_{N_E} \} \begin{bmatrix} \mathbf{1} \ \mathbf{0} \ \mathbf{0} \ \mathbf{0} \ \mathbf{Z} \ -\mathbf{H} \ \mathbf{0} \ \mathbf{Z} \ \mathbf{H} \ \Xi \ \mathbf{0} \ \mathbf{0} \\ \mathbf{0} \ \mathbf{1} \ \mathbf{0} \ -\mathbf{Z} \ \mathbf{0} \ \Xi \ \mathbf{Z} \ \mathbf{0} \ \Xi \ \mathbf{0} \ \mathbf{H} \ \mathbf{0} \\ \mathbf{0} \ \mathbf{0} \ \mathbf{1} \ \mathbf{H} \ -\Xi \ \mathbf{0} \ \mathbf{H} \ \Xi \ \mathbf{0} \ \mathbf{0} \ \mathbf{0} \ \mathbf{Z} \end{bmatrix}, \quad (26)$$

where  $\mathbf{1}$  is a  $N_E \times 1$  column vector of ones,  $\mathbf{0}$  is a  $N_E \times 1$  column vector of zeros, and  $\Xi = \{ \xi_1 \ \xi_2 \ \dots \ \xi_{N_E} \}^T$ ,  $\mathbf{H} = \{ \eta_1 \ \eta_2 \ \dots \ \eta_{N_E} \}^T$ ,  $\mathbf{Z} = \{ \zeta_1 \ \zeta_2 \ \dots \ \zeta_{N_E} \}^T$  are the nodal values of the affine functions  $\xi$ ,  $\eta$  and  $\zeta$ , respectively, which are defined in (5).

On using (26), we have

$$\Pi^\epsilon \boldsymbol{\varphi} = \widehat{\mathbf{M}} \boldsymbol{\Pi}_*^\epsilon = \boldsymbol{\varphi} \mathbf{D} \boldsymbol{\Pi}_*^\epsilon, \quad (27a)$$

and therefore

$$\boldsymbol{\Pi}^\epsilon := \mathbf{D} \boldsymbol{\Pi}_*^\epsilon \quad (27b)$$

is the matrix representation of the projection in the  $\boldsymbol{\varphi}$  basis set.

We define a mean discrete  $L^2$  inner product on the element  $E$  as:

$$P_0(\mathbf{u}^h, \mathbf{v}^h) := \frac{1}{N_E} \sum_{k=1}^{N_E} \mathbf{u}^h(\mathbf{x}_k) \cdot \mathbf{v}^h(\mathbf{x}_k) = \frac{1}{N_E} \sum_{i=1}^{3N_E} \text{dof}_i(\mathbf{u}^h) \text{dof}_i(\mathbf{v}^h). \quad (28)$$

Now, from (10), the variational problem to determine the projector can be written as

$$a_E^h(\mathbf{m}_\alpha, \Pi^\epsilon \mathbf{v}^h) = a_E^h(\mathbf{m}_\alpha, \mathbf{v}^h) \quad \text{for } \mathbf{m}_\alpha \in \widehat{\mathbf{M}} \ (\alpha = 7, 8, \dots, 12), \quad (29a)$$

$$P_0(\mathbf{m}_\alpha, \Pi^\epsilon \mathbf{v}^h)_{\partial E} = P_0(\mathbf{m}_\alpha, \mathbf{v}^h)_{\partial E} \quad \text{for } \mathbf{m}_\alpha \in \widehat{\mathbf{M}} \ (\alpha = 1, 2, \dots, 6). \quad (29b)$$

On substituting  $\mathbf{v}^h = \boldsymbol{\varphi}_i$  ( $i = 1, 2, \dots, 3N_E$ ) in (29) and using (28), we have

$$a_E^h(\mathbf{m}_\alpha, \Pi^\varepsilon \boldsymbol{\varphi}_i) = a_E^h(\mathbf{m}_\alpha, \boldsymbol{\varphi}_i) \quad \text{for } \mathbf{m}_\alpha \in \widehat{\mathbf{M}} \quad (\alpha = 7, 8, \dots, 12), \quad (30a)$$

$$\frac{1}{N_E} \sum_{j=1}^{3N_E} \text{dof}_j(\mathbf{m}_\alpha) \text{dof}_j(\Pi^\varepsilon \boldsymbol{\varphi}_i) = \frac{1}{N_E} \sum_{j=1}^{3N_E} \text{dof}_j(\mathbf{m}_\alpha) \text{dof}_j(\boldsymbol{\varphi}_i) \quad \text{for } \mathbf{m}_\alpha \in \widehat{\mathbf{M}} \quad (\alpha = 1, 2, \dots, 6). \quad (30b)$$

Equation (30b) equates the average value of  $\boldsymbol{\varphi}_i$  and that of its projection along the coordinate directions (rigid-body translations for  $\alpha = 1, 2, 3$ ) and likewise for the infinitesimal rigid-body rotations about the  $x$ -,  $y$ -, and  $z$ -axes ( $\alpha = 4, 5, 6$ ).

On using (23), (30a) becomes

$$\begin{aligned} \sum_{\beta=1}^{12} a_E^h(\mathbf{m}_\alpha, \mathbf{m}_\beta) s_\beta^i &= a_E^h(\mathbf{m}_\alpha, \boldsymbol{\varphi}_i) \quad (\alpha = 7, 8, \dots, 12) \\ &= \int_E \boldsymbol{\sigma}(\mathbf{m}_\alpha) : \boldsymbol{\varepsilon}(\boldsymbol{\varphi}_i) \, d\mathbf{x} \\ &= \int_E \nabla \cdot (\boldsymbol{\varphi}_i \cdot \boldsymbol{\sigma}(\mathbf{m}_\alpha)) \, d\mathbf{x} - \int_E (\nabla \cdot \boldsymbol{\sigma}(\mathbf{m}_\alpha)) \cdot \boldsymbol{\varphi}_i \, d\mathbf{x} \\ &= \int_{\partial E} \mathbf{t}(\mathbf{m}_\alpha) \cdot \boldsymbol{\varphi}_i \, dS = \sum_{\mathbf{f} \subset \partial E} \mathbf{t}_{\mathbf{f}}(\mathbf{m}_\alpha) \cdot \int_{\mathbf{f}} \Pi_{\mathbf{f}}^\varepsilon \boldsymbol{\varphi}_i \, dS, \end{aligned}$$

where the divergence theorem has been invoked and we have used the fact that  $\nabla \cdot \boldsymbol{\sigma}(\mathbf{m}_\alpha) = \mathbf{0}$  since  $\mathbf{m}_\alpha$  are affine fields. In addition,  $\mathbf{t}_{\mathbf{f}}(\mathbf{m}_\alpha)$  is the traction vector on  $\mathbf{f}$  and  $\Pi_{\mathbf{f}}^\varepsilon$  is the projection operator on  $\mathbf{f}$ . The three vectorial basis functions that are associated with node  $K$  can be expressed as  $\boldsymbol{\varphi}_K := \phi_K \mathbf{I}_3$  ( $\phi_K$  is the scalar canonical basis function). Since finite elements with only triangular faces are considered in Section 6, then  $\Pi_{\mathbf{f}}^\varepsilon \boldsymbol{\varphi}_K = \boldsymbol{\varphi}_K = \phi_K \mathbf{I}_3$  ( $\phi_K$  is an affine function on a triangle,  $\triangle$ ) and a one-point Gauss rule delivers exact integration on each face. If so, then

$$\sum_{\beta=1}^{12} a_E^h(\mathbf{m}_\alpha, \mathbf{m}_\beta) s_\beta^K = \sum_{\mathbf{f}=\triangle} \mathbf{t}_{\mathbf{f}}(\mathbf{m}_\alpha) \cdot \int_{\mathbf{f}} \phi_K \mathbf{I}_3 \, dS = \frac{1}{3} \sum_{\mathbf{f}=\triangle} \mathbf{t}_{\mathbf{f}}(\mathbf{m}_\alpha) |\mathbf{f}| \quad (\alpha = 7, 8, \dots, 12). \quad (31)$$

On substituting for  $\Pi^\varepsilon \boldsymbol{\varphi}_i$  from (23) in (30b), we obtain

$$\frac{1}{N_E} \sum_{j=1}^{3N_E} \sum_{\beta=1}^{12} \text{dof}_j(\mathbf{m}_\alpha) \text{dof}_j(\mathbf{m}_\beta) s_\beta^K = \frac{1}{N_E} \sum_{j=1}^{3N_E} \text{dof}_j(\mathbf{m}_\alpha) \text{dof}_j(\boldsymbol{\varphi}_K) \quad (\alpha = 1, 2, \dots, 6). \quad (32)$$

Using Voigt notation, let  $\widetilde{\mathbf{B}} = \boldsymbol{\varepsilon}(\widehat{\mathbf{M}})$  be the  $6 \times 12$  matrix that represents the symmetric gradient of the column vectors of  $\widehat{\mathbf{M}}$  in (6) and  $\mathbf{C}$  be the  $6 \times 6$  constitutive matrix for an isotropic linear elastic solid. Also, let  $\boldsymbol{\sigma}^* = \mathbf{C} \widetilde{\mathbf{B}}$  be the  $6 \times 12$  matrix representation of the stress tensor of the displacement fields in  $\widehat{\mathbf{M}}$ ; then the traction on a face  $\mathbf{f}$  is  $\mathbf{t}_{\mathbf{f}} = \mathbf{n}_{\mathbf{f}} \cdot \boldsymbol{\sigma}^*$ . In (31),  $a_E^h(\mathbf{m}_\alpha, \mathbf{m}_\beta) = \int_E \boldsymbol{\sigma}(\mathbf{m}_\alpha) : \boldsymbol{\varepsilon}(\mathbf{m}_\beta) \, d\mathbf{x} = \boldsymbol{\sigma}(\mathbf{m}_\alpha) : \boldsymbol{\varepsilon}(\mathbf{m}_\beta) |E| = \widetilde{\mathbf{B}}^T \mathbf{C} \widetilde{\mathbf{B}} |E|$ . Further, on noting that  $\text{dof}_i(\mathbf{m}_\alpha) = \mathbf{D}_{i\alpha}$ ,  $\text{dof}_j(\boldsymbol{\varphi}_i) = \delta_{ij}$  and recalling that  $\mathbf{S} := \Pi_*$  is the matrix of unknown coefficients, the linear system that stems from (32) and (31) can be written as:

$$\mathbf{G} \Pi_* = \widehat{\mathbf{B}}, \quad \Pi_* = \mathbf{G}^{-1} \widehat{\mathbf{B}}, \quad (33a)$$

where

$$\tilde{\mathbf{G}} = \tilde{\mathbf{B}}^T \mathbf{C} \tilde{\mathbf{B}} |E|, \quad \mathbf{G} = \tilde{\mathbf{G}}, \quad \mathbf{G}(1:6, :) = \frac{[\mathbf{D}^T \mathbf{D}](1:6, :)}{N_E}, \quad (33b)$$

$$\hat{\mathbf{B}}(1:6, :) = \frac{[\mathbf{D}(:, 1:6)]^T}{N_E}, \quad \hat{\mathbf{B}}(7:12, :) = \frac{1}{3} \sum_{\mathbf{f}=\Delta C \partial E} [(\boldsymbol{\sigma}^*)^T \mathbf{n}_f](7:12, :) |f|. \quad (33c)$$

## 5.2 | Element stiffness matrix

The expression for the element stiffness matrix is:

$$\begin{aligned} \mathbf{K}_E &= a_E^h(\boldsymbol{\varphi}, \boldsymbol{\varphi}) \\ &= a_E^h(\Pi^\epsilon \boldsymbol{\varphi} + (1 - \Pi^\epsilon) \boldsymbol{\varphi}, \Pi^\epsilon \boldsymbol{\varphi} + (1 - \Pi^\epsilon) \boldsymbol{\varphi}) \\ &= a_E^h(\Pi^\epsilon \boldsymbol{\varphi}, \Pi^\epsilon \boldsymbol{\varphi}) + a_E^h((1 - \Pi^\epsilon) \boldsymbol{\varphi}, (1 - \Pi^\epsilon) \boldsymbol{\varphi}) \\ &= a_E^h(\widehat{\mathbf{M}} \Pi_*^\epsilon, \widehat{\mathbf{M}} \Pi_*^\epsilon) + a_E^h(\boldsymbol{\varphi}(\mathbf{I} - \Pi^\epsilon), \boldsymbol{\varphi}(\mathbf{I} - \Pi^\epsilon)) \\ &= (\Pi_*^\epsilon)^T a_E^h(\widehat{\mathbf{M}}, \widehat{\mathbf{M}}) \Pi_*^\epsilon + (\mathbf{I} - \Pi^\epsilon)^T a_E^h(\boldsymbol{\varphi}, \boldsymbol{\varphi}) (\mathbf{I} - \Pi^\epsilon), \end{aligned}$$

where we recall that  $\Pi^\epsilon = \mathbf{D} \Pi_*^\epsilon$ ,  $\mathbf{I}$  is the  $dN_E \times dN_E$  identity matrix, and the third equality is reached since the cross terms vanish due to the orthogonality condition in (10a). The first (consistency) term in  $\mathbf{K}_E$  is computable whereas  $a_E^h(\boldsymbol{\varphi}, \boldsymbol{\varphi})$  in the second (stability) term is not computable. To ensure coercivity of  $\mathbf{K}_E$ , we approximate this term by a diagonal matrix,  $\mathbf{S}_E^d$ , with the appropriate magnitude (scaling). Effective choices for this diagonal matrix (so-called D-recipe) have been investigated,<sup>8,9</sup> and tailored for elastodynamics in Park et al.<sup>14</sup> The entries in the diagonal matrix are chosen as:  $(\mathbf{S}_E^d)_{ii} = \max(\alpha_0 \operatorname{tr}(\mathbf{C})/m, (\mathbf{K}_E^c)_{ii})$ , where  $m = 3$  in 2D and  $m = 6$  in 3D, and  $\alpha_0 = 1$  in 2D and  $\alpha_0 = h_E$  is used in 3D. On setting  $a_E^h(\boldsymbol{\varphi}, \boldsymbol{\varphi}) \approx \mathbf{S}_E^d$ , both the consistency and stability matrices are now computable:

$$\mathbf{K}_E^c = (\Pi_*^\epsilon)^T a_E^h(\widehat{\mathbf{M}}, \widehat{\mathbf{M}}) \Pi_*^\epsilon = (\Pi_*^\epsilon)^T \left( \int_E \boldsymbol{\sigma}(\widehat{\mathbf{M}}) : \boldsymbol{\epsilon}(\widehat{\mathbf{M}}) d\mathbf{x} \right) \Pi_*^\epsilon = (\Pi_*^\epsilon)^T \tilde{\mathbf{G}} \Pi_*^\epsilon, \quad \mathbf{K}_E^s = (\mathbf{I} - \Pi^\epsilon)^T \mathbf{S}_E^d (\mathbf{I} - \Pi^\epsilon). \quad (34)$$

Hence, the element stiffness matrix is:

$$\mathbf{K}_E = \mathbf{K}_E^c + \mathbf{K}_E^s = (\Pi_*^\epsilon)^T \tilde{\mathbf{G}} \Pi_*^\epsilon + (\mathbf{I} - \Pi^\epsilon)^T \mathbf{S}_E^d (\mathbf{I} - \Pi^\epsilon). \quad (35)$$

## 5.3 | Element mass matrix

We now use the  $L^2$  projection operator to derive the element mass matrix. For  $k = 1$ , the  $L^2$  and the elliptic projector coincide:  $\Pi^0 = \Pi^\nabla$ .<sup>6</sup> Both satisfy the equality conditions given in (12), and hence the equivalence. So on computing the elliptic projection operator we can use its matrix representation to construct the element mass matrix. The  $\Pi^\nabla$  elliptic projector has appeared extensively in the VEM literature; for the sake of completeness, we present the derivation with the most important steps.

Again, let  $\boldsymbol{\varphi}_K = \phi_K \mathbf{I}_d$  represent  $d$  vectorial basis functions that are associated with node  $K$ . Referring to (14), let the elliptic (vector Laplacian) projection of the vectorial basis functions be represented as:

$$\Pi^\nabla \boldsymbol{\varphi}_K = \Pi^\nabla(\phi_K \otimes \mathbf{I}_d) = \Pi^\nabla \phi_K \otimes \mathbf{I}_d = \left( \sum_{\beta=1}^{d+1} m_\beta s_\beta^K \right) \otimes \mathbf{I}_d, \quad (K = 1, 2, \dots, N_E), \quad m_\beta \in \widehat{\mathbf{m}}_0, \quad (36)$$

where  $\widehat{\mathbf{m}}_0 = \{1, \xi, \eta\}$  if  $d = 2$  and  $\widehat{\mathbf{m}}_0 = \{1, \xi, \eta, \zeta\}$  if  $d = 3$ , and  $\mathbf{S}_0 := \{s^1 s^2 \dots s^{N_E}\}$  is the matrix of unknown coefficients. Define the dof-matrix,  $\mathbf{D}_0 = \text{dof}_i(m_\alpha)$ , as

$$\mathbf{D}_0 = [\mathbf{1} \ \Xi \ \mathbf{H}] \quad (d = 2), \quad \mathbf{D}_0 = [\mathbf{1} \ \Xi \ \mathbf{H} \ \mathbf{Z}] \quad (d = 3). \quad (37)$$

On using  $\mathbf{q} = m_\alpha \otimes \mathbf{I}_d$  and  $\mathbf{v} := \mathbf{v}^h = \boldsymbol{\varphi}_K = \phi_K \otimes \mathbf{I}_d$  in (8), the variational problem to determine the elliptic projector becomes

$$a_E^h(\mathbf{I}_d \otimes m_\alpha, \Pi^\nabla(\phi_K \otimes \mathbf{I}_d)) = a_E^h(\mathbf{I}_d \otimes m_\alpha, \phi_K \otimes \mathbf{I}_d), \quad \text{for } m_\alpha \in \widehat{\mathbf{m}}_0 \setminus 1 \quad (38a)$$

$$P_0(\mathbf{I}_d \otimes m_\alpha, \Pi^\nabla(\phi_K \otimes \mathbf{I}_d))_{\partial E} = P_0(\mathbf{I}_d \otimes m_\alpha, \phi_K \otimes \mathbf{I}_d)_{\partial E} \quad \text{for } m_\alpha = 1, \quad (38b)$$

where  $K = 1, 2, \dots, N_E$ , and the projector  $P_0(\cdot, \cdot)$  is defined in (28). On using (36) and (28), we can rewrite (38) as

$$\mathbf{I}_d \otimes a_E^h \left( m_\alpha, \sum_{\beta} m_\beta s_\beta^K \right) \otimes \mathbf{I}_d = \mathbf{I}_d \otimes a_E^h(m_\alpha, \phi_K) \otimes \mathbf{I}_d, \quad \text{for } m_\alpha \in \widehat{\mathbf{m}}_0 \setminus 1 \quad (39a)$$

$$\mathbf{I}_d \otimes \left( \frac{1}{N_E} \sum_{j=1}^{N_E} \sum_{\beta} \text{dof}_j(m_\alpha) \text{dof}_j(m_\beta) s_\beta^K \right) \otimes \mathbf{I}_d = \mathbf{I}_d \otimes \left( \frac{1}{N_E} \sum_{j=1}^{N_E} \text{dof}_j(m_\alpha) \text{dof}_j(\phi_K) \right) \otimes \mathbf{I}_d \quad \text{for } m_\alpha = 1. \quad (39b)$$

In (39), the bilinear form,  $a_E(u, v) = \int_E \nabla u \cdot \nabla v \, d\mathbf{x}$ , is associated with the scalar Laplace operator. From (39), we now obtain

$$\begin{aligned} \sum_{\beta} \int_E \nabla m_\alpha \cdot \nabla m_\beta \, d\mathbf{x} s_\beta^K &= \int_E \nabla m_\alpha \cdot \nabla \phi_K \, d\mathbf{x} \\ &= \int_E \nabla \cdot (\phi_K \nabla m_\alpha) \, d\mathbf{x} - \int_E \phi_K \nabla^2 m_\alpha \, d\mathbf{x} \\ &= \int_{\partial E} \phi_K (\nabla m_\alpha \cdot \mathbf{n}) \, dS \\ &= \sum_{\mathbf{f} \subset \partial \Omega} \int_{\mathbf{f}} \Pi_{\mathbf{f}}^\nabla \phi_K (\nabla m_\alpha \cdot \mathbf{n}_{\mathbf{f}}) \, dS \quad \text{for } m_\alpha \in \widehat{\mathbf{m}}_0 \setminus 1, \end{aligned} \quad (40a)$$

and

$$\frac{1}{N_E} \sum_{j=1}^{N_E} \sum_{\beta} \text{dof}_j(m_\alpha) \text{dof}_j(m_\beta) s_\beta^K = \frac{1}{N_E} \sum_{j=1}^{N_E} \delta_{jK} = \frac{1}{N_E} \quad \text{for } m_\alpha = 1, \quad (40b)$$

where  $\nabla^2 m_\alpha = 0$  is used to reach (40a),  $\text{dof}_j(m_\alpha) = 1$  for  $m_\alpha = 1$ , and  $\text{dof}_j(\phi_K) = \delta_{jK}$ . Now,

$$\nabla \widehat{\mathbf{m}}_0 = \begin{bmatrix} 0 & \mathbf{0}^T \\ \mathbf{0} & \frac{\mathbf{I}_d}{h_E} \end{bmatrix}, \quad (41)$$

where  $\mathbf{0}$  is a  $d$ -dimensional column vector of zeros. Let  $\mathbf{S}_0 = \{s^1 \ s^2 \ \dots \ s^{N_E}\}$  be the matrix of unknown coefficients. Then, using the expressions for  $\mathbf{D}_0$  and  $\nabla \widehat{\mathbf{m}}_0$  in (40), we solve for the projection matrix  $\mathbf{S}_0$  using the following linear system of equations:

$$\mathbf{G}_0 \mathbf{S}_0 = \widehat{\mathbf{B}}_0, \quad \mathbf{S}_0 = \mathbf{G}_0^{-1} \widehat{\mathbf{B}}_0, \quad (42a)$$

$$\mathbf{G}_0(1, :) = \frac{\mathbf{D}_0^T \mathbf{D}(1, :)}{N_E}, \quad \mathbf{G}_0(2 : d+1, :) = \frac{|E|}{h_E^2} \mathbf{I}_d, \quad (42b)$$

$$\widehat{\mathbf{B}}_0(1, :) = \frac{\mathbf{D}_0^T(1, :)}{N_E} = \frac{\mathbf{1}}{N_E}, \quad \widehat{\mathbf{B}}_0(2 : d+1, :) = \sum_{\mathbf{f} \subset \partial E} \frac{\mathbf{n}_{\mathbf{f}} |\mathbf{f}|}{dh_E}, \quad (42c)$$

where  $\mathbf{1}$  is a  $N_E$ -dimensional row vector of ones and we have assumed that the boundary faces  $\mathbf{f}$  are simplices in  $\mathbb{R}^d$  so that  $\int_{\mathbf{f}} \Pi_{\mathbf{f}}^{\nabla} \phi_K dS = \int_{\mathbf{f}} \phi_K dS = |\mathbf{f}|/d$ . Now, we can write the matrix representations of the  $L^2$  projection operators (identical to the  $\Pi^{\nabla}$  projection operators) with respect to the scaled vectorial basis,  $\widehat{\mathbf{m}}_0 \otimes \mathbf{I}_d$ , and the canonical vectorial basis,  $\boldsymbol{\phi} \otimes \mathbf{I}_d$ , as

$$\Pi_*^0 = \mathbf{S}_0 \otimes \mathbf{I}_d \quad \text{and} \quad \Pi^0 = [\mathbf{D}_0 \otimes \mathbf{I}_d] \Pi_*^0, \quad (43)$$

respectively. Proceeding as we did for the stiffness matrix, on using (4b) we can write the element mass matrix as

$$\begin{aligned} \mathbf{M}_E &= b_E^h(\boldsymbol{\varphi}, \boldsymbol{\varphi}) \\ &= b_E^h(\Pi^0 \boldsymbol{\varphi} + (1 - \Pi^0) \boldsymbol{\varphi}, \Pi^0 \boldsymbol{\varphi} + (1 - \Pi^0) \boldsymbol{\varphi}) \\ &= b_E^h(\Pi^0 \boldsymbol{\varphi}, \Pi^0 \boldsymbol{\varphi}) + b_E^h((1 - \Pi^0) \boldsymbol{\varphi}, (1 - \Pi^0) \boldsymbol{\varphi}) \\ &= b_E^h(\widehat{\mathbf{M}}_0 \Pi_*^0, \widehat{\mathbf{M}}_0 \Pi_*^0) + b_E^h(\boldsymbol{\varphi}(I - \Pi^0), \boldsymbol{\varphi}(I - \Pi^0)) \\ &= (\Pi_*^0)^T b_E^h(\widehat{\mathbf{M}}_0, \widehat{\mathbf{M}}_0) \Pi_*^0 + (I - \Pi^0)^T b_E^h(\boldsymbol{\varphi}, \boldsymbol{\varphi}) (I - \Pi^0) \\ &\approx (\Pi_*^0)^T \mathbf{H}_0 \Pi_*^0 + \rho |E| (I - \Pi^0)^T (I - \Pi^0) \\ &:= \mathbf{M}_E^c + \mathbf{M}_E^s, \end{aligned} \quad (44)$$

where  $\widehat{\mathbf{M}}_0 = \widehat{\mathbf{m}}_0 \otimes \mathbf{I}_d$ ,  $\mathbf{H}_0$  is a matrix of integrals of monomials up to order 2, which are listed in (55), and we approximate  $b_E^h(\boldsymbol{\varphi}, \boldsymbol{\varphi})$  by  $\rho |E|$  in the stabilization term.

### 5.3.1 | Lumped mass matrix

We perform mass lumping to construct diagonal mass matrices using row-sum and diagonal scaling techniques. In the row-sum technique,<sup>31</sup> the diagonal entries of the lumped mass matrix is given by

$$M_{E,ii}^{\ell} = \sum_{j=1}^{dN_E} M_{E,ij} \quad (d = 2, 3). \quad (45)$$

The diagonal entries of the lumped mass matrix using the diagonal scaling procedure are given by<sup>32</sup>

$$M_{E,ii}^\ell = \frac{M_{E,ii}}{\text{trace}(\mathbf{M}_E)} d\rho|E|, \quad (46)$$

which ensures that mass conservation is satisfied ( $\rho|E|$  is the mass in each direction). Diagonal scaling always leads to lumped mass matrices with positive diagonal entries, which is not guaranteed with the row-sum technique. For convex polyhedral elements, we use the row-sum lumped mass technique, and for nonconvex polyhedral elements the diagonally-scaled lumped mass matrix is used.<sup>14,15</sup>

#### 5.4 | Estimation of critical time step

For stable explicit linear elastodynamic simulations, the time step increment is subject to a restriction, which is given by the CFL condition:

$$\Delta t \leq \frac{2}{\omega_{\max}}, \quad (47)$$

where  $\omega_{\max}$  is the maximum natural frequency of vibration of the elastic solid. The natural frequency is related to the eigenvalue  $\lambda$  of the generalized eigenproblem,

$$\mathbf{K}d = \lambda \mathbf{M}d, \quad (48)$$

by the relation  $\lambda = \omega^2 \geq 0$ . By the element-eigenvalue inequality,<sup>26</sup> we have  $\omega^* = \max(\omega_E^{\max}) \geq \omega_{\max}$ , and therefore a conservative lower bound estimate for the stable critical time step is given by

$$\Delta t_{\text{crit}} = \frac{2}{\omega^*} \leq \frac{2}{\omega_{\max}}. \quad (49)$$

#### 5.5 | Homogeneous numerical integration scheme

The homogeneous numerical integration (HNI) scheme<sup>33</sup> allows to reduce integration of homogeneous functions over arbitrary convex and nonconvex polytopes to integration over the boundary facets of the polytope. Let  $f(\mathbf{x})$  be a positively homogeneous function of degree  $q$  that is continuously differentiable:

$$f(\lambda \mathbf{x}) = \lambda^q f(\mathbf{x}) \quad (\lambda > 0), \quad (50)$$

which satisfies Euler's homogeneous function theorem:

$$qf(\mathbf{x}) = (\nabla f(\mathbf{x}), \mathbf{x}) \quad \forall \mathbf{x} \in \mathbb{R}^d, \quad (51)$$

where  $(\cdot, \cdot)$  denotes the inner product of vectors in  $\mathbb{R}^d$  and  $\mathbf{x}$  is the position vector in  $\mathbb{R}^d$ .



Consider a polyhedral element  $E$ . The generalized Stokes's (divergence) theorem over  $E$  can be stated as:

$$\int_E (\nabla \cdot \mathbf{X}) f(\mathbf{x}) d\mathbf{x} + \int_E (\mathbf{X}, \nabla f(\mathbf{x})) d\mathbf{x} = \int_{\partial E} (\mathbf{X}, \mathbf{n}) f(\mathbf{x}) d\sigma, \quad (52)$$

where  $d\sigma$  is the Lebesgue measure on  $\partial E$ . For a homogeneous function  $f$  and letting  $\mathbf{X} := \mathbf{x}$  be a vector field and noting that  $\nabla \cdot \mathbf{x} = d$ , (52) reduces to

$$\int_E f(\mathbf{x}) d\mathbf{x} = \frac{1}{d+q} \sum_{i=1}^m \frac{b_i}{\|\mathbf{a}_i\|} \int_{\mathfrak{f}_i} f(\mathbf{x}) d\sigma, \quad (53)$$

where  $\partial E = \cup_{i=1}^m \mathfrak{f}_i$  consists of  $m$  planar polygonal faces. Each  $\mathfrak{f}_i$  is a subset of the hyperplane  $\mathcal{H}_i = \{\mathbf{x} : \mathbf{a}_i \cdot \mathbf{x} = b_i\}$ .

On reapplying Stokes's theorem and Euler's homogeneous function theorem on  $\mathfrak{f}_i \subset \mathcal{H}_i$ , we can write<sup>33</sup>

$$\int_{\mathfrak{f}_i} f(\mathbf{x}) d\sigma = \frac{1}{d+q-1} \left[ \sum_{j \neq i} \int_{\mathfrak{f}_{ij}} d_{ij} f(\mathbf{x}) d\nu + \int_{\mathfrak{f}_i} (\nabla f(\mathbf{x}), \mathbf{x}_0) d\sigma \right], \quad (54)$$

where  $\mathbf{x}_0 \in \mathcal{H}_i$  is an arbitrary point that satisfies  $\mathbf{a}_i \cdot \mathbf{x}_0 = b_i$ ,  $\mathfrak{f}_{ij} \subset \mathcal{H}_{ij} = \mathfrak{f}_i \cap \mathfrak{f}_j$  is the  $(d-2)$ -dimensional facet, and  $d_{ij} := (\mathbf{x} - \mathbf{x}_0, \mathbf{n}_{ij})$  is the algebraic distance from  $\mathbf{x}_0$  to  $\mathcal{H}_{ij}$ .

For the first-order VEM ( $k=1$ ), we require the computation of integrals over  $E$  that involve monomials of maximum order 1 for the stiffness matrix and monomials of maximum order 2 for the mass matrix. We compute all such integrals by using a bottom-up approach, starting from the zeroth order monomial (volume computation) to order 2. In doing so, previously stored values are used to evaluate the second term (integral of monomials over the faces of the polyhedra) on the right-hand side of (54). This leads to exact computation of these integrals.<sup>34</sup> Referring to (5), we use HNI to compute the following integrals:

$$\begin{aligned} \int_E d\mathbf{x} &= |E|, \quad \int_E \xi d\mathbf{x} = \frac{1}{h_E} \left[ \int_E x d\mathbf{x} - x_E |E| \right], \quad \int_E \eta d\mathbf{x} = \frac{1}{h_E} \left[ \int_E y d\mathbf{x} - y_E |E| \right], \quad \int_E \zeta d\mathbf{x} = \frac{1}{h_E} \left[ \int_E z d\mathbf{x} - z_E |E| \right], \\ \int_E \xi \eta d\mathbf{x} &= \frac{1}{h_E^2} \left[ \int_E xy d\mathbf{x} - y_E \int_E x d\mathbf{x} - x_E \int_E y d\mathbf{x} + x_E y_E |E| \right], \\ \int_E \xi \zeta d\mathbf{x} &= \frac{1}{h_E^2} \left[ \int_E xz d\mathbf{x} - z_E \int_E x d\mathbf{x} - x_E \int_E z d\mathbf{x} + x_E z_E |E| \right], \\ \int_E \eta \zeta d\mathbf{x} &= \frac{1}{h_E^2} \left[ \int_E yz d\mathbf{x} - z_E \int_E y d\mathbf{x} - y_E \int_E z d\mathbf{x} + y_E z_E |E| \right], \\ \int_E \xi^2 d\mathbf{x} &= \frac{1}{h_E^2} \left[ \int_E x^2 d\mathbf{x} - 2x_E \int_E x d\mathbf{x} + x_E^2 |E| \right], \\ \int_E \eta^2 d\mathbf{x} &= \frac{1}{h_E^2} \left[ \int_E y^2 d\mathbf{x} - 2y_E \int_E y d\mathbf{x} + y_E^2 |E| \right], \\ \int_E \zeta^2 d\mathbf{x} &= \frac{1}{h_E^2} \left[ \int_E z^2 d\mathbf{x} - 2z_E \int_E z d\mathbf{x} + z_E^2 |E| \right], \end{aligned} \quad (55)$$

**TABLE 1** Critical time step in 2D for FEM (Delaunay meshes) and VEM using lumped (row-sum) mass matrix. For the VEM, bad triangles (interior angle close to  $0^\circ$ ) are agglomerated with neighboring triangles to form a polygonal element.

Mesh	Method	$E$		$E$		$\frac{\Delta t_{\text{crit}}^{\text{VEM}}}{\Delta t_{\text{crit}}^{\text{FEM}}}$
			$\omega_{\text{max}}^E$		$\omega_{\text{max}}^E$	
1a ( $\epsilon = 10^{-1}$ )	FEM	1	$1.5 \times 10^5$	3	$2.0 \times 10^4$	$\sim 4$
1b ( $\epsilon = 10^{-1}$ )	VEM	1	$3.6 \times 10^4$	2	$2.0 \times 10^4$	
1c ( $\epsilon = 10^{-2}$ )	FEM	1	$1.5 \times 10^6$	3	$1.9 \times 10^4$	$\sim 30$
1d ( $\epsilon = 10^{-2}$ )	VEM	1	$4.9 \times 10^4$	2	$1.9 \times 10^4$	
1e ( $\epsilon = 10^{-5}$ )	FEM	1	$1.5 \times 10^9$	3	$1.9 \times 10^4$	$\sim 10^4$
1f ( $\epsilon = 10^{-5}$ )	VEM	1	$5.1 \times 10^4$	2	$1.9 \times 10^4$	
$\epsilon = 10^{-8}$	FEM	1	$1.5 \times 10^{12}$	3	$1.9 \times 10^4$	$\sim 10^7$
$\epsilon = 10^{-8}$	VEM	1	$5.1 \times 10^4$	2	$1.9 \times 10^4$	

where  $|E|$  is the volume of the polyhedral element  $E$ .

## 6 | NUMERICAL RESULTS

We use the element-eigenvalue inequality to obtain an estimate of the critical time step for linear elastodynamic simulations. FEM is executed on Delaunay meshes and VEM is adopted on polyhedra that are formed via agglomeration of tetrahedral and prismatic elements. In all computations, material properties of steel are used:  $E_Y = 210$  GPa,  $\nu = 0.3$  and  $\rho = 7800$  kg/m<sup>3</sup>.

### 6.1 | Two-dimensional study

We assume plane strain conditions and consider sequence of finite element meshes in which the length of the smallest edge is monotonically decreased ( $\epsilon = 10^{-1}, 10^{-2}, 10^{-5}, 10^{-8}$ ). Three meshes from this sequence for FE and VEM (polygonal meshes) are presented in Fig. 1. The results for the maximum natural frequency as well as the improvements in  $\Delta t_{\text{crit}}$  that are obtained using VEM are listed in Table 1. The second element serves as a reference since this element is well-shaped (right-angled nearly isosceles triangle). The overall maximum frequency on the FE meshes increases substantially from  $1.5 \times 10^5$  Hz to  $1.5 \times 10^{12}$  Hz, whereas for the VEM the increase is from  $3.6 \times 10^4$  Hz to  $5.1 \times 10^4$  Hz. For the VEM, the maximum frequency is relatively insensitive to the minimum edge length. On using the VEM on agglomerated element much larger time steps can be used in comparison to the FEM, with a factor of 4 when  $\epsilon = 1$  to a factor of  $10^7$  when  $\epsilon = 10^{-8}$ .

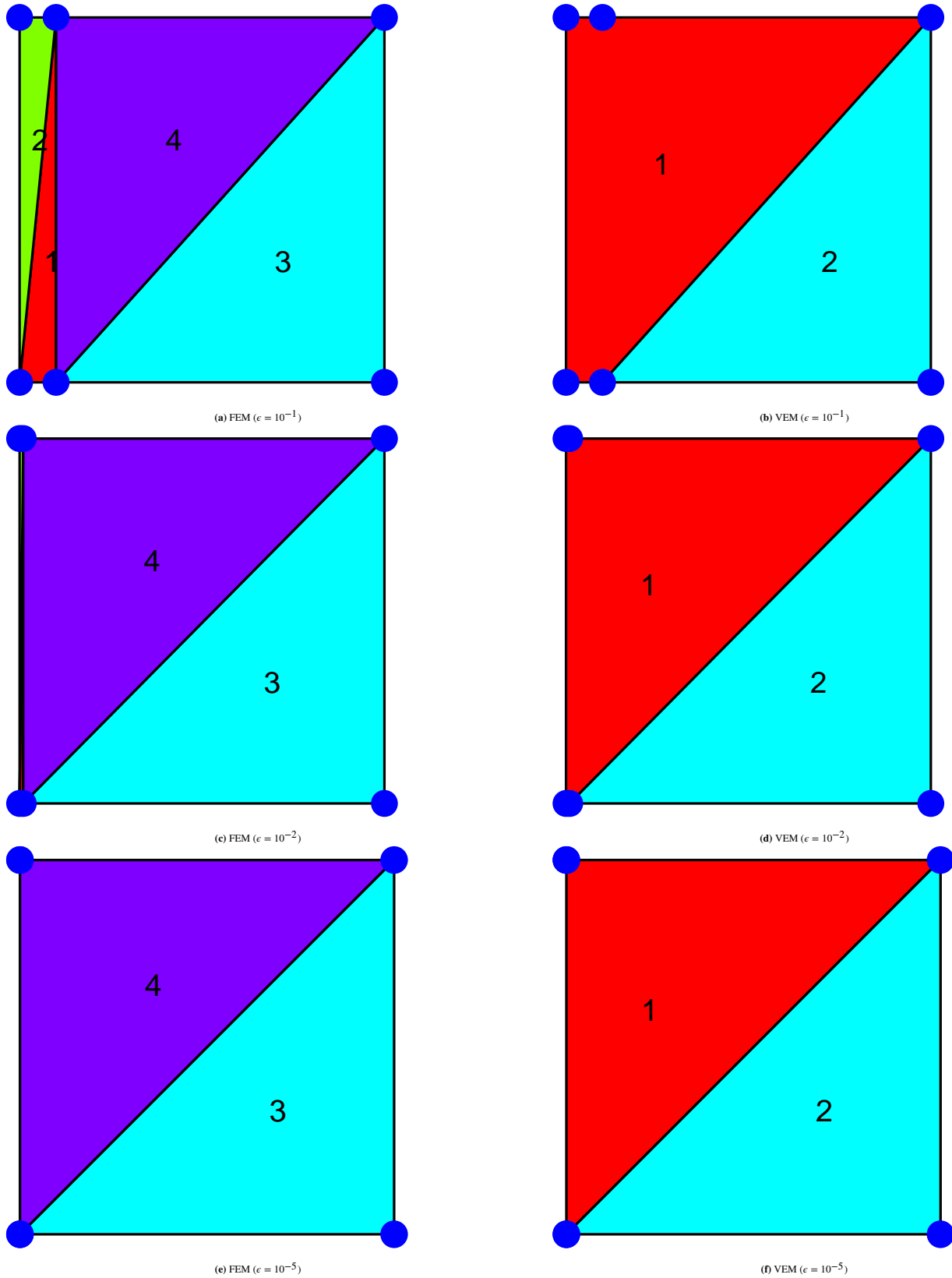


**FIGURE 1** Triangular finite element and polygonal meshes that are used to determine the critical time step.

**TABLE 2** Critical time step using lumped (row-sum) mass matrix for stretched prismatic finite elements and agglomerated virtual elements. For the virtual element computations, prismatic elements with vanishing face areas are agglomerated with their neighbors to create a hexahedral element with many triangular faces.

Mesh	Method	$E$	$\omega_{\max}^E$ (Hz)	$E$	$\omega_{\max}^E$ (Hz)	$\frac{\Delta t_{\text{crit}}^{\text{VEM}}}{\Delta t_{\text{crit}}^{\text{FEM}}}$
2a ( $\epsilon = 10^{-1}$ )	FEM	1	$1.7 \times 10^5$	3	$2.6 \times 10^4$	$\sim 3$
2b ( $\epsilon = 10^{-1}$ )	VEM	1	$4.9 \times 10^4$	2	$2.6 \times 10^4$	
2c ( $\epsilon = 10^{-5}$ )	FEM	1	$1.7 \times 10^9$	3	$2.5 \times 10^4$	$\sim 10^4$
2d ( $\epsilon = 10^{-5}$ )	VEM	1	$1.0 \times 10^5$	2	$2.5 \times 10^4$	

## 6.2 | Three-dimensional study

We consider one case with prismatic elements and then three cases that contain poor-quality tetrahedral elements. For the prismatic element, we use the row-sum technique to form the lumped mass matrix, whereas for the polyhedral elements (in general, nonconvex polyhedra) that are formed by agglomerating sliver (kite) and spire tetrahedra, diagonal scaling is used to form the lumped mass matrix. In the 3D study, since we use meshes with elements whose diameters are  $\mathcal{O}(1)$ , we set  $\alpha_0 = 1$  in the stabilization term of the stiffness matrix.

### 6.2.1 | Prismatic elements

The mesh that was considered in two dimensions is extended to three dimensions by extruding the two-dimensional meshes in the third dimension, which results in prismatic elements. The agglomeration is done in a similar manner as in 2D. Two polyhedral virtual elements are created and the polygonal faces are represented as the union of triangular faces. Meshes for FE and VEM are presented in Fig. 2, and the results for the maximum natural frequency as well as the ratio of  $\Delta t_{\text{crit}}$  obtained using VEM and FEM are listed in Table 2. The trends are similar to the 2D case. The faces with very small areas do not affect the maximum frequency in the virtual element computations.

### 6.2.2 | Tetrahedral elements

Tetrahedral meshes with wedge, kite configuration and spires are considered.<sup>35</sup> Agglomeration of a badly-shaped tetrahedral element with a neighboring element is performed to construct a polyhedral virtual element that is used in the computations.

**Wedge tetrahedron.** Consider the two-element tetrahedral configuration shown in Fig. 3a. The tetrahedral element above the  $xy$ -plane is a wedge tetrahedron (one dihedral angle is close to  $0^\circ$ ) with  $\epsilon$  being the  $z$ -coordinate of the node above the  $xy$ -plane. The tetrahedral element below the  $xy$ -plane is well-shaped. The meshes shown in Fig. 3 are for  $\epsilon = 10^{-1}$ . The two elements are

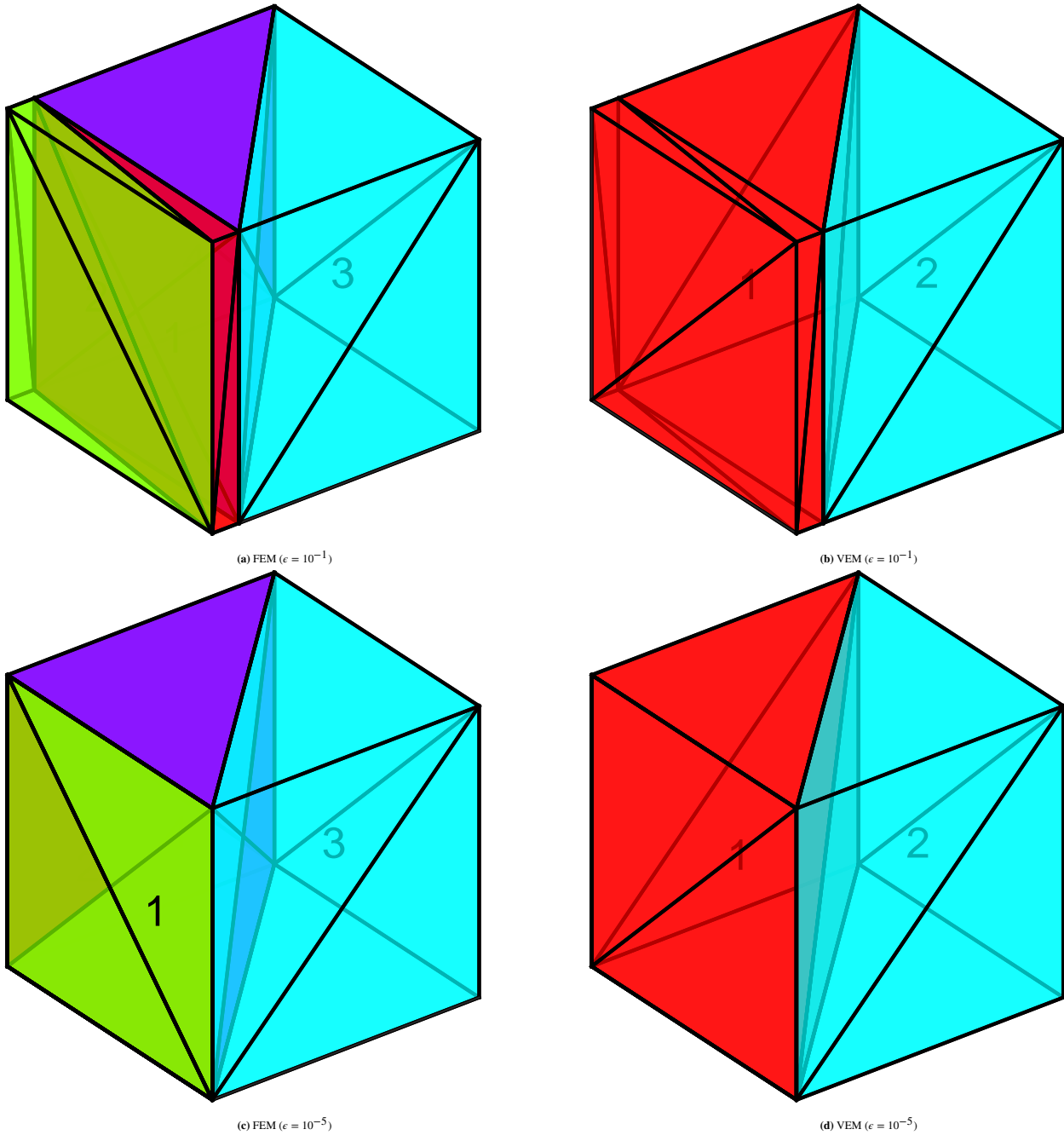


**FIGURE 2** Prismatic meshes (FEM) and polyhedral meshes (triangular faces) used in the study to determine the critical time step.

combined to form a single polyhedral element with six faces (see Fig. 3b). Numerical results for the maximum natural frequency for  $\epsilon = 10^{-1}$ ,  $10^{-3}$ ,  $10^{-5}$  and the ratio of the critical time step for VEM to that obtained using the FEM are listed in Table 3. For  $\epsilon = 10^{-5}$ , the ratio of the critical time step of VEM to that of FEM is  $\mathcal{O}(10^4)$ .

**Sliver (kite) tetrahedron.** We consider a sliver (kite) tetrahedron element. The coordinates of the nodes of this tetrahedron are:  $(-1, 0, \epsilon)$ ,  $(1, 0, \epsilon)$ ,  $(0, -1, -\epsilon)$ , and  $(0, 1, \epsilon)$ . Two dihedral angles of this tetrahedron are close to  $180^\circ$ , and the other four

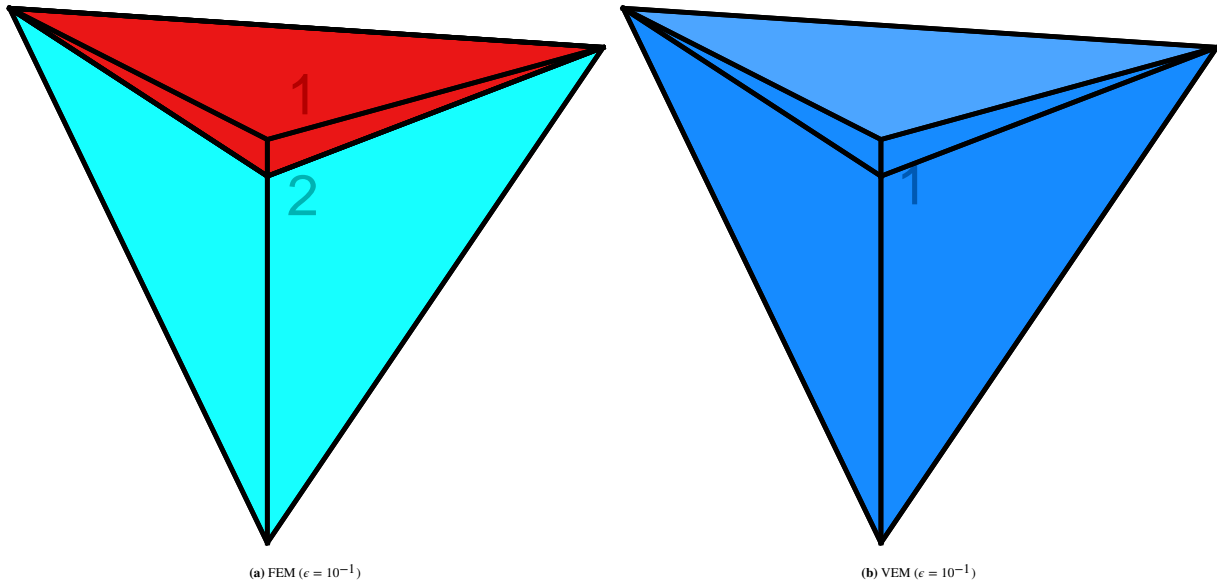


**FIGURE 3** Influence of a wedge tetrahedral element on the critical time step. (a) Two tetrahedral finite elements with one of them being a wedge. (b) Agglomeration of the two tetrahedral elements into a single polyhedral virtual element.

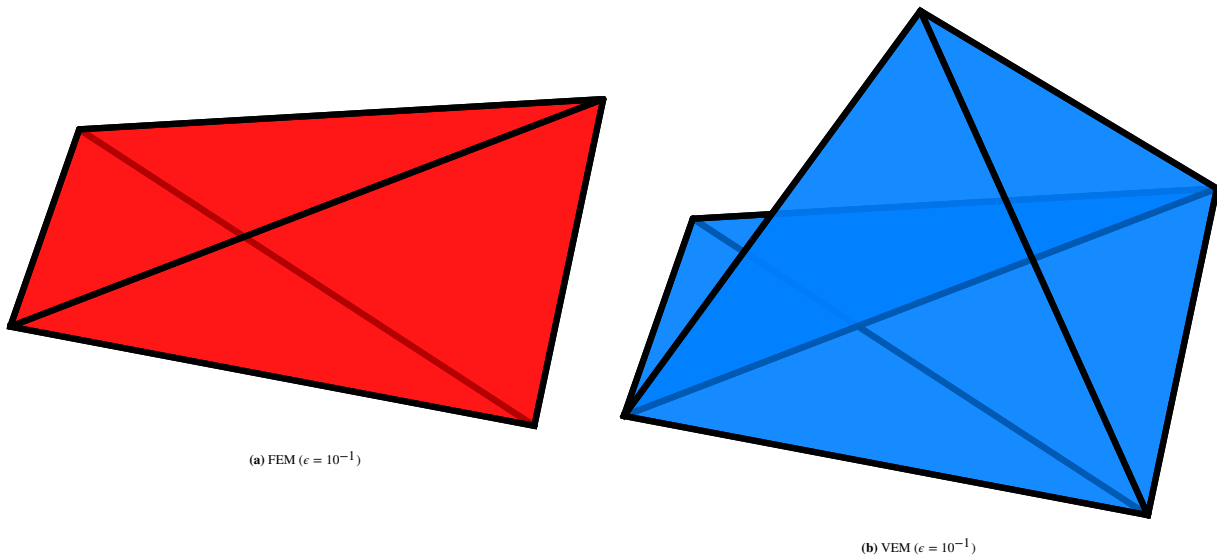


**FIGURE 4** Influence of tetrahedral kite element on the critical time step. (a) Tetrahedral kite element and (b) Agglomeration of the kite element with a neighboring tetrahedral element to form a polyhedral virtual element.

dihedral angles are close to  $0^\circ$ . We join this tetrahedron to a neighboring tetrahedron with the additional vertex  $(0, 0, 1)$  to form a polyhedral (nonconvex) virtual element. The kite tetrahedron and the polyhedral virtual element are shown in Fig. 4.

Numerical results for the maximum natural frequency for  $\epsilon = 10^{-1}$ ,  $10^{-5}$ , and the ratio of the critical time step for VEM to that obtained using the FEM are listed in Table 4. We observe that for  $\epsilon = 10^{-5}$ , the critical time step estimate for the VEM polyhedral element is four orders greater than that of FEM. As  $\epsilon$  decrease this ratio increases; the critical step in the VEM is insensitive to  $\epsilon$ . As  $\epsilon \rightarrow 0$ , the stable time step for the VEM is of the same order as a well-shaped tetrahedral finite element.

**TABLE 3** Critical time step using lumped (diagonal scaling) mass matrix for tetrahedral finite elements with a wedge and an agglomerated virtual element. The agglomerated virtual element has six triangular faces.

$\epsilon$	Method	$E$	$\omega_{\max}^E$ (Hz)	$E$	$\omega_{\max}^E$ (Hz)	$\frac{\Delta t_{\text{crit}}^{\text{VEM}}}{\Delta t_{\text{crit}}^{\text{FEM}}}$
$10^{-1}$	FEM	1	$1.7 \times 10^5$	2	$2.5 \times 10^4$	$\sim 3$
	VEM	1	$4.3 \times 10^4$	–	–	
$10^{-3}$	FEM	1	$1.7 \times 10^7$	2	$2.5 \times 10^4$	$\sim 10^2$
	VEM	1	$4.6 \times 10^4$	–	–	
$10^{-5}$	FEM	1	$1.7 \times 10^9$	2	$2.5 \times 10^4$	$\sim 10^4$
	VEM	1	$4.6 \times 10^4$	–	–	

**TABLE 4** Critical time step using lumped (diagonal scaling) mass matrix for a tetrahedral kite finite element and an agglomeration of it with a neighboring elements into a polyhedral (nonconvex) virtual element. The agglomerated virtual element has six triangular faces.

$\epsilon$	Method	$\omega_{\max}^{\text{FEM}}$ (Hz)	Method	$\omega_{\max}^{\text{VEM}}$ (Hz)	$\frac{\Delta t_{\text{crit}}^{\text{VEM}}}{\Delta t_{\text{crit}}^{\text{FEM}}}$
$10^{-1}$	FEM	$6.0 \times 10^4$	VEM	$3.1 \times 10^4$	$\sim 2$
$10^{-5}$	FEM	$6.0 \times 10^8$	VEM	$5.2 \times 10^4$	$\sim 10^4$

**Spire tetrahedron.** We consider a spire tetrahedron, which is a tetrahedron with one tiny face and three long edges. The nodal coordinates of this tetrahedron are chosen as:  $(0, 0, 0)$ ,  $(0, \epsilon, 0)$ ,  $(0, 0, \epsilon)$ , and  $(1, 0, 0)$ . For the neighboring tetrahedron, we consider the vertices  $(0, 0, -1)$ ,  $(0, -1, 0)$  and  $(1/2, 1, 0)$ . We join the spire tetrahedron with one or two neighboring tetrahedra to form a polyhedral virtual element. Three such cases are considered that we label as *A*, *B*, and *C*. For  $\epsilon = 10^{-1}$ , the spire tetrahedron and the polyhedral virtual element (cases *A*, *B*, and *C*) that are formed via agglomeration are shown in Fig. 5.

Numerical results for the maximum natural frequency for  $\epsilon = 10^{-1}$ ,  $10^{-5}$ , and the ratio of the critical time step for VEM (cases *A*, *B* and *C*) vis-à-vis FEM are listed in Table 5. For cases *A* and *B* with the virtual element (severly distorted nonconvex

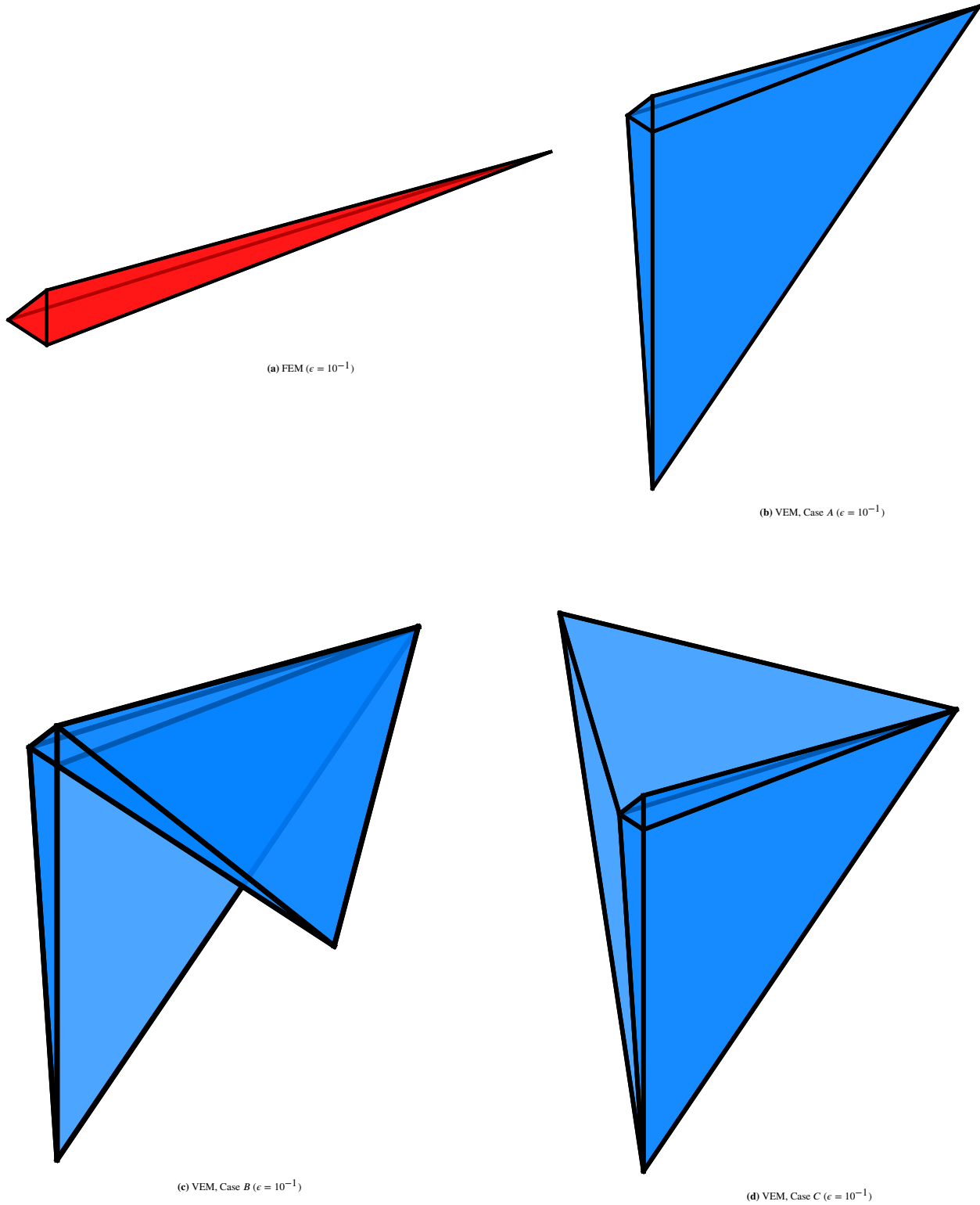


**FIGURE 5** Influence of tetrahedral spire element on the critical time step. (a) Tetrahedral spire element. Agglomeration of the spire with (b) one neighboring element (case *A*), and (c), (d) two neighboring elements (cases *B* and *C*) to form a polyhedral virtual element.



**TABLE 5** Critical time step using lumped (diagonal scaling) mass matrix for a tetrahedral spire finite element and an agglomeration of it with neighboring elements into a polyhedral (nonconvex) virtual element.

$\epsilon$	Method	$\omega_{\max}^{\text{FEM}}$ (Hz)	Method	$\omega_{\max}^{\text{VEM}}$ (Hz)	$\frac{\Delta t_{\text{crit}}^{\text{VEM}}}{\Delta t_{\text{crit}}^{\text{FEM}}}$
$10^{-1}$	FEM	$2.2 \times 10^5$	VEM (Case A)	$3.2 \times 10^5$	$\sim 1$
			VEM (Case B)	$3.9 \times 10^5$	$\sim 1$
			VEM (Case C)	$5.5 \times 10^4$	$\sim 6$
$10^{-5}$	FEM	$2.2 \times 10^9$	VEM (Case A)	$3.3 \times 10^9$	$\sim 1$
			VEM (Case B)	$2.2 \times 10^{13}$	$\sim 10^{-4}$
			VEM (Case C)	$5.9 \times 10^4$	$\sim 10^4$

elements), the critical time step is appreciably greater than that for the FEM. For case *C* (nearly convex element), the VEM outperforms the FEM, and the trends are similar to results for other problems that are reported earlier. For  $\epsilon = 10^{-5}$ , the critical time step estimate for the VEM polyhedral element (case *C*) is four orders greater than that of FEM. We find that as  $\epsilon \rightarrow 0$ , the stable time step for this case is of the same order as a well-shaped tetrahedral finite element. For instance, if  $\epsilon = 10^{-8}$ , we find that  $\omega_{\max}^{\text{VEM}} = 5.9 \times 10^5$  Hz. To promote better conditioning of the stiffness matrix, it is preferable to agglomerate with more neighbors to produce a polyhedral virtual element with nonvanishing volume.

### 6.3 | Explicit dynamics simulations on a tapered beam

To establish the robustness and efficiency of meshes with agglomerated polyhedral virtual elements over poor-quality tetrahedral finite element meshes, we present elastodynamic simulations for a manufactured problem. To this end, we begin with a two-dimensional beam of dimensions  $[0, 4] \times [0, 1]$  that is meshed with bilinear finite elements. We cut this mesh with an inclined line that results in some elements having poor quality. For FEM, all 2D elements are split into triangles. For VEM, there are uncut hexahedral elements as well as polygonal (greater than four edges) elements that are formed as agglomerations of the triangles. Sample two-dimensional meshes of the tapered beam are shown in Fig. 6. These meshes are extruded (one element thickness) in the  $z$ -direction. The 2D triangular elements yield prismatic elements in 3D. Each prism is meshed into three tetrahedral elements. This results in poor-quality tetrahedra in some of the regions in the vicinity of the cut plane. For the virtual element analysis, the elements are hexahedra away from the cutting plane. Near the cutting plane the 2D triangles are aggregated into polygons as shown, then extruded in  $z$  to form polyhedral virtual elements. Every rectangular face of the 3D extrusions is partitioned into two triangles. Each hexahedral virtual element has 12 triangular faces, whereas each agglomerated virtual element has 20 triangular faces.

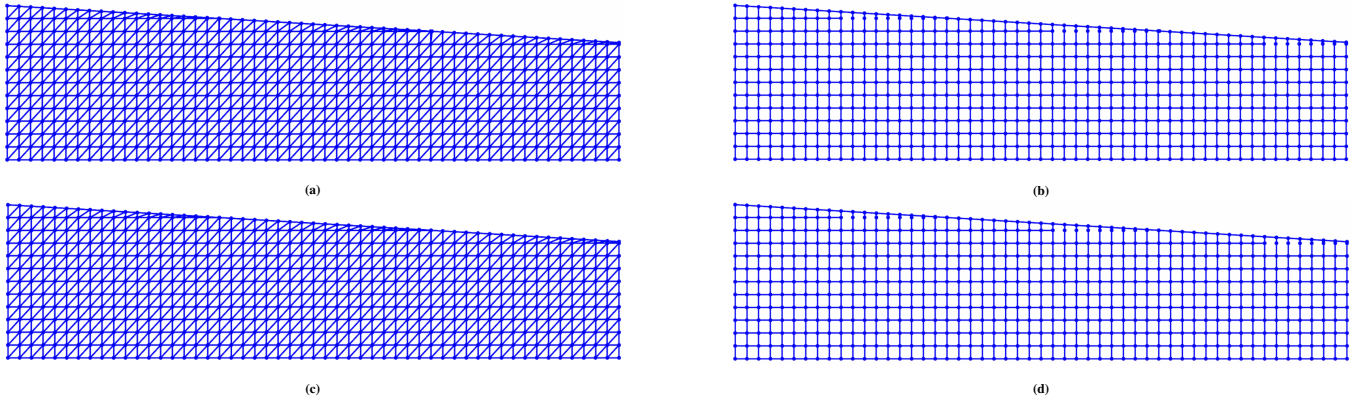


**FIGURE 6** Two-dimensional meshes of the tapered beam, which are constructed by cutting a structured mesh by a line. (a), (b) Triangular and polygonal meshes (Case *A*); and (c), (d) Triangular and polygonal meshes (Case *B*).

Three-dimensional meshes are generated by extruding the two-dimensional meshes shown in Fig. 6. We refer to case *A* as the meshes shown in Fig. 6a and Fig. 6b, whereas case *B* refers to the meshes shown in Fig. 6c and Fig. 6d. Though not visible at the scale shown, the cut line is distinct in each case, with case *B* designed to result in sliver tetrahedra of poorer quality when compared to case *A*. For cases *A* and *B*, the number of nodes and elements for the tetrahedral meshes (and likewise for the polyhedral meshes) are the same. The number of nodes in all meshes is 1282. The number of elements in the tetrahedral finite element mesh is 3456 and that in the polyhedral virtual element mesh is 549. The estimates for the maximum natural frequency in cases *A* and *B* are listed in Table 6. In Fig. 9b (case *B*), since  $\omega_{\max}^{FEM} = \mathcal{O}(10^{16})$ , the global system (stiffness and lumped mass) matrices ( $\mathbf{Kd} = \omega^2 \mathbf{Md}$ ) are used to compute the maximum frequency in the FE simulations (see Table 6). For cases *A* and *B*, the critical time step in the VEM is 275 and  $4.5 \times 10^4$  times larger than the critical time step in the FEM, respectively.

**TABLE 6** Critical time step for FEM and VEM in the explicit dynamics simulations.

Meshes	$\omega_{\max}^{FEM}$ (Hz)	$\omega_{\max}^{VEM}$ (Hz)	$\frac{\Delta t_{\text{crit}}^{VEM}}{\Delta t_{\text{crit}}^{FEM}}$
Case A	$8.0 \times 10^7$	$2.9 \times 10^5$	275
Case B	$1.3 \times 10^{10*}$	$2.9 \times 10^5$	$4.5 \times 10^4$

\*Maximum natural frequency is based on the global elastodynamic eigenproblem

In Fig. 7, the surface triangular elements for case *A* are depicted along with the 3D polyhedral virtual elements that have 20 faces. The tetrahedron with the worst condition number and the agglomerated polyhedron virtual element (20 faces) that contains the vertices of this tetrahedron are shown in Figures 8a and 8b, respectively.

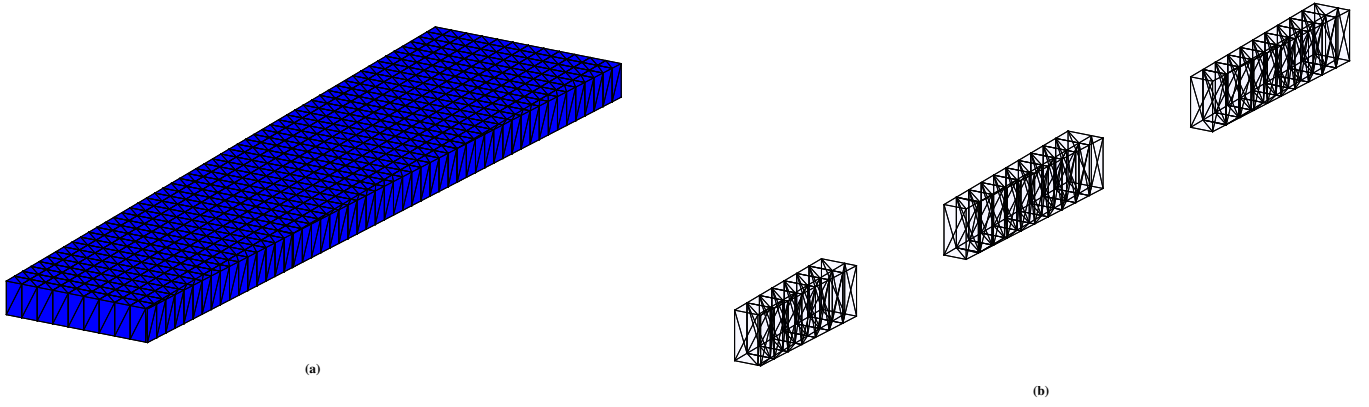


**FIGURE 7** (a) Surface triangular elements for tetrahedral and polyhedral virtual element meshes and (b) Agglomerated polyhedral virtual elements that have 20 faces.

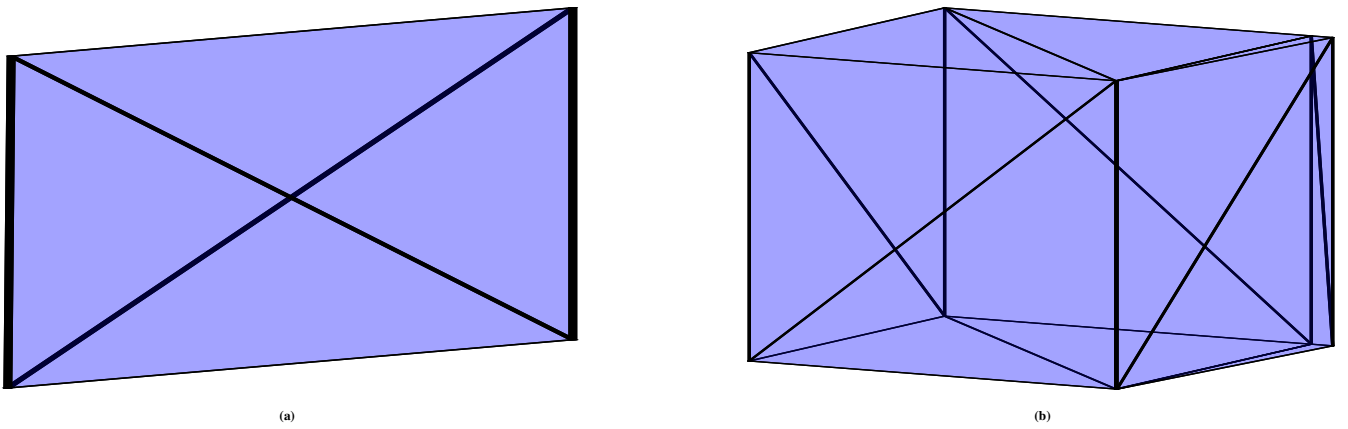


**FIGURE 8** Plots of elements from case A. (a) Poor-quality tetrahedron and (b) Agglomeration of the same tetrahedron with its neighbor to form a polyhedral virtual element.

Let  $\mathbf{u} \equiv (u(\mathbf{x}, t), v(\mathbf{x}, t), w(\mathbf{x}, t))$  be the displacement field and  $\boldsymbol{\sigma} \equiv \boldsymbol{\sigma}(x, y, z, t)$  be the Cauchy stress field. For the tapered beam, we solve the following elastodynamic initial/boundary-value problem:

$$\nabla \cdot \boldsymbol{\sigma} = \rho \ddot{\mathbf{u}} \quad \text{in } \Omega \times [0, T_{\max}] \quad (56a)$$

$$\mathbf{u}(x, y, z, 0) = 0, \quad \dot{\mathbf{u}}(x, y, z, 0) = 0, \quad (56b)$$

$$\mathbf{u}(0, y, z, t) = 0, \quad v(4, y, z, t) = 0, \quad w(4, y, z, t) = 0, \quad (56c)$$

$$u(4, y, z, t) = \begin{cases} \left(\frac{t}{\tau}\right)^4 - 2\left(\frac{t}{\tau}\right)^3 + \left(\frac{t}{\tau}\right)^2 & \text{for } t < \tau \\ 0 & \text{otherwise} \end{cases}, \quad (56d)$$

where we choose  $\tau = 100\Delta t_{\text{crit}}^{\text{VEM}}$  in the numerical simulations. In addition, we set Poisson's ratio  $\nu = 0$  to produce a two-dimensional solution for the wave propagation problem.

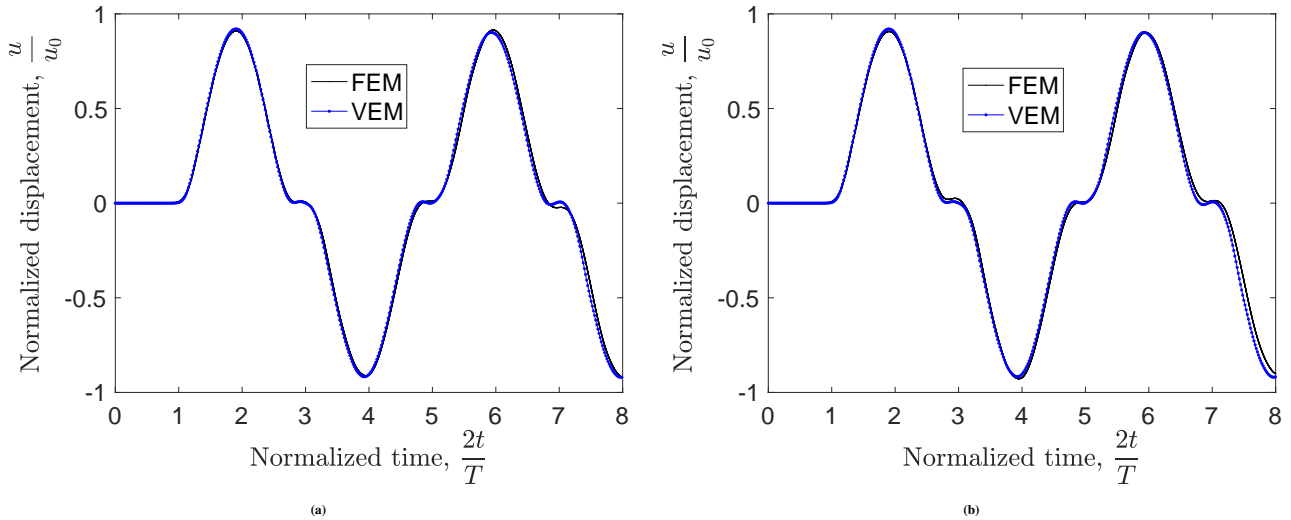


**FIGURE 9** Time history of the normalized displacement in the  $x$ -direction. Comparisons of FE and virtual element solutions for the meshes in case  $A$  (Figures 6a and 6b) are shown in (a). Solutions for the meshes in case  $B$  (Figures 6c and 6d) are shown in (b). In (b), the speed-up of virtual element simulation versus FEM is of  $\mathcal{O}(10^4)$ .

In the numerical computations, an explicit central-difference scheme is used for the time integration.<sup>31</sup> We normalize the displacement in the  $x$ -direction by  $u_0 = 1/16$  and the time by  $T = 4/c_L = 7.7 \times 10^{-4}$ , where  $c_L = 5188.75$  m/s is the longitudinal wave speed. In Fig. 9, the time history of the normalized displacement in the  $x$ -direction at the nodal location  $(2, 1/2, 0)$  is presented. We observe that the virtual element and finite element solutions are in good agreement. In Fig. 9a (case  $A$ ), the critical time step of the VEM is 275 times that of the critical time step in the FEM. In Fig. 9b (case  $B$ ), the speed-up of the virtual element simulation (453 time steps) over finite elements (20.9 million time steps) is of  $\mathcal{O}(10^4)$ . For this problem, we point out that it is impractical to use the element-eigenvalue inequality to set the time step, which further reinforces the advantages of VEM. We emphasize that in both the FEM and VEM meshes there are nearly co-located nodes connected by an edge with an extremely small length compared to the average element size. It is known that the stable time step in the FEM is highly dependent on this edge length; however, it is remarkable that the stable time step in the VEM is essentially independent of it. Finally, we point out that consistent with expectations, instability in the time history of the FE solution is observed when  $\Delta t_{\text{FEM}} = 1.000001 \Delta t_{\text{crit}}^{\text{FEM-g}}$ .

## 7 | CONCLUSIONS

In this paper, we adopted the first-order virtual element method to increase the critical time step for linear elastodynamic finite element simulations on tetrahedral meshes that contain poor-quality elements (small faces and dihedral angles close to  $0^\circ$  and/or  $180^\circ$ ). We considered tetrahedra with wedge, sliver and spire elements.<sup>35</sup> To this end, we agglomerated poorly-shaped prismatic and tetrahedral elements with their neighbors into polyhedral virtual elements to estimate the critical time step. Lumped mass

matrices using row-sum (diagonal scaling) technique for convex (nonconvex) polyhedral elements were utilized.<sup>14</sup> The element-eigenvalue inequality<sup>26,27,31</sup> was used to provide an estimate of the critical time step. For prismatic, wedge and sliver elements, we found that agglomeration with neighboring tetrahedra into polyhedral elements (with finite volume) produced critical time steps that were insensitive as the mesh parameter  $\epsilon \rightarrow 0$ . For spire tetrahedral elements, agglomeration produced mixed results: poor performance resulted when the volume of the polyhedral virtual element approached zero as  $\epsilon \rightarrow 0$ , but for an agglomerated polyhedral virtual element with finite volume, the critical time step was found to be insensitive as  $\epsilon \rightarrow 0$ . Notably, in the favorable instances, the ratio of the critical time step of the polyhedral virtual element to that of the badly-shaped finite element was  $\mathcal{O}(\epsilon^{-1})$ , which increases as  $\epsilon \rightarrow 0$ . This observation suggests that agglomeration should be done with neighboring elements so that the polyhedral volume does not vanish as  $\epsilon \rightarrow 0$ . Lastly, we presented explicit dynamics simulations on a three-dimensional tapered beam to demonstrate that the increase in critical time step using polyhedral virtual elements leads to significantly faster computer simulations when compared to tetrahedral finite elements.

This study has shown the promise of virtual element technology to enable accurate and reliable linear elastodynamic finite element simulations on low-quality tetrahedral meshes. Future work will focus on studying the influence of polyhedral shape quality measures on the eigenspectrum and exploring robust approaches to perform agglomeration of poor-quality tetrahedra into polyhedral virtual elements for elastodynamic simulations.

## ACKNOWLEDGEMENTS

NS acknowledges the research support of Sandia National Laboratories to the University of California at Davis. The authors thank Eric Chin for providing the code to numerically integrate monomials over polytopes using the homogeneous numerical integration method. Helpful discussions with Franco Dassi are also gratefully acknowledged. Sandia National Laboratories is a multimission laboratory managed and operated by National Technology and Engineering Solutions of Sandia, LLC, a wholly owned subsidiary of Honeywell International, Inc., for the U.S. Department of Energy's National Nuclear Security Administration under contract DE-NA-0003525. This paper describes objective technical results and analysis. Any subjective views or opinions that might be expressed in the paper do not necessarily represent the views of the U.S. Department of Energy or the United States Government.

## References

1. Hormann K, Sukumar N., eds. *Generalized Barycentric Coordinates in Computer Graphics and Computational Mechanics*. Boca Raton: Taylor & Francis, CRC Press . 2017.

2. Beirão da Veiga L, Brezzi F, Cangiani A, Manzini G, Marini LD, Russo A. Basic principles of virtual element methods. *Math Models Methods Appl Sci* 2013; 23: 119–214.
3. Beirão da Veiga L, Lipnikov K, Manzini G. *The Mimetic Finite Difference Method for Elliptic Problems*. 11 of *MS&A – Modeling, Simulation and Applications*. Cham: Springer . 2014.
4. Flanagan DP, Belytschko T. A uniform strain hexahedron and quadrilateral with orthogonal hourglass control. *Int J Numer Methods Eng* 1981; 17(5): 679–706.
5. Cangiani A, Manzini G, Russo A, Sukumar N. Hourglass stabilization and the virtual element method. *Int J Numer Methods Eng* 2015; 102(3–4): 404–436.
6. Ahmad B, Alsaedi A, Brezzi F, Marini LD, Russo A. Equivalent projectors for virtual element methods. *Comput Math Applications* 2013; 66: 376–391.
7. Beirão da Veiga L, Brezzi F, Marini LD, Russo A. The hitchhiker’s guide to the virtual element method. *Math Models Methods Appl Sci* 2014; 24(8): 1541–1573.
8. Beirão da Veiga L, Dassi F, Russo A. High-order Virtual Element Method on polyhedral meshes. *Comput Math Applications* 2017; 74: 1110–1122.
9. Dassi F, Mascotto L. Exploring high-order three dimensional virtual elements: Bases and stabilizations. *Comput Math Applications* 2018; 75(9): 3379–3401.
10. Beirão da Veiga L, Brezzi F, Marini D. Virtual elements for linear elasticity problems. *SIAM J Numer Anal* 2013; 51(2): 794–812.
11. Gain AL, Talischi C, Paulino GH. On the Virtual Element Method for three-dimensional linear elasticity problems on arbitrary polyhedral meshes. *Comput Methods Appl Mech Eng* 2014; 282: 132–160.
12. Artioli E, Beirão da Veiga L, Lovadina C, Sacco E. Arbitrary order 2D virtual elements for polygonal meshes: part I, elastic problem. *Comput Mech* 2017; 60(3): 355–377.
13. Mengolini M, Benedetto MF, Aragón AM. An engineering perspective to the virtual element method and its interplay with the standard finite element method. *Comput Methods Appl Mech Eng* 2019; 350: 995–1023.
14. Park K, Chi H, Paulino GH. On nonconvex meshes for elastodynamics using virtual element methods with explicit time integration. *Comput Methods Appl Mech Eng* 2019; 356: 669–684.

15. Park K, Chi H, Paulino GH. Numerical recipes for elastodynamic virtual element methods with explicit time integration. *Int J Numer Methods Eng* 2020; 121(1): 1–31.
16. Antonietti PF, Manzini G, Mazzieri I, Mourad HM, Verani M. The arbitrary-order virtual element method for linear elastodynamics models: convergence, stability and dispersion-dissipation analysis. *Int J Numer Methods Eng* 2021; 122(4): 934–971.
17. Cihan M, Aldakheel F, Hudobivnik B, Wriggers P. Virtual element formulation for finite strain elastodynamics. arXiv preprint: 2002.02680; 2020.
18. Koester JJ, Tupek MR, Mitchell SA. An agile design-to-simulation workflow using a new conforming moving least squares method. Tech. Rep. SAND2019-11851, Sandia National Laboratories; Albuquerque, NM 87185, USA: 2019.
19. Bassi F, Botti L, Colombo A, Petro DAD, Tesini P. On the flexibility of agglomeration based physical space discontinuous Galerkin discretizations. *J Comput Phys* 2012; 231(1): 45–65.
20. Cangiani A, Georgoulis EH, Houston P. *hp*-version discontinuous Galerkin methods on polygonal and polyhedral meshes. *Math Models Methods Appl Sci* 2014; 24(10): 2009–2041.
21. Bishop JE, Sukumar N. Polyhedral finite elements for nonlinear solid mechanics using tetrahedral subdivisions and dual-cell aggregation. *Comput Aided Geom Des* 2020; 77: 101812.
22. Shewchuk JR. What is a good linear finite element? Interpolation, conditioning, anisotropy, and quality measures (preprint). Department of Computer Science, University of California, Berkeley, CA 94720, USA; 2002.
23. Klingner BM. *Improving Tetrahedral Meshes*. PhD thesis. Department of Electrical Engineering and Computer Sciences, University of California, Berkeley, CA 94720, USA; 2008.
24. Gillette A, Rand A. Shape quality for generalized barycentric interpolation. in Hormann and Sukumar<sup>1</sup>ch. 2: 23–42.
25. Attene M, Biasotti S, Bertoluzza S, et al. Benchmarking the geometrical robustness of a Virtual Element Poisson solver. *Math Comput Simulation* 2021; 190: 1392–1414.
26. Fried I. Bounds on the extremal eigenvalues of the finite element stiffness and mass matrices and their spectral condition numbers. *Journal of Sound and Vibration* 1972; 22(4): 407–418.
27. Lin JJ. An element eigenvalue theorem and its application for stable time steps. *Comput Methods Appl Mech Eng* 1989; 73: 283–294.
28. Lin JJ. Bounds on eigenvalues of finite element systems. *Int J Numer Methods Eng* 1991; 32: 957–967.

29. Benvenuti E, Chiozzi A, Manzini G, Sukumar N. Extended virtual element method for the Laplace problem with singularities and discontinuities. *Comput Methods Appl Mech Eng* 2019; 356: 571–597.
30. Vacca G, Beirão da Veiga L. Virtual element methods for parabolic problems on polygonal meshes. *Numer Meth Part D E* 2015; 31(6): 2110–2134.
31. Hughes TJR. *The Finite Element Method: Linear Static and Dynamic Finite Element Analysis*. Mineola, NY: Dover Publications, Inc. . 2000.
32. Hinton E, Rock T, Zienkiewicz OC. A note on mass lumping and related processes in the finite element method. *Earthquake Engineering & Structural Dynamics* 1976; 4(3): 245–249.
33. Chin EB, Lasserre JB, Sukumar N. Numerical integration of homogeneous functions on convex and nonconvex polygons and polyhedra. *Comput Mech* 2015; 56(6): 967–981.
34. Chin EB, Sukumar N. An efficient method to integrate polynomials over polytopes and curved solids. *Comput Aided Geom Des* 2020; 82: 101914.
35. Cheng SW, Dey TK, Edelsbrunner H, Facello MA, Teng SH. Sliver exudation. *Journal of the ACM* 2000; 47(5): 883–904.

